X-ray magnetic dichroism in III-V diluted magnetic semiconductors: First-principles calculations

V. N. Antonov,[1,2] A. N. Yaresko,[1] and O. Jepsen[1]
[1]*Max-Planck-Institut für Festkörperforschung, Heisenberg Strasse 1, D-70569 Stuttgart, Germany*
[2]*Institute of Metal Physics, 36 Vernadsky Street, 03142 Kiev, Ukraine*
(Received 4 June 2009; revised manuscript received 30 November 2009; published 16 February 2010)

The electronic structure of the (Ga,Mn)As, (Ga,Mn)N, and (Ga,Gd)N, diluted magnetic semiconductors (DMSs) were investigated theoretically from first principles, using the fully relativistic Dirac linear muffin-tin orbital band-structure method. The electronic structure is obtained with the local spin-density approximation (LSDA), as well as the LSDA+U method. The x-ray magnetic circular and linear dichroism (XMCD and XMLD) spectra at the Mn, As, Ga, and N K and Gd, Mn, As, and Ga $L_{2,3}$ edges were investigated theoretically from first principles. The origin of the XMCD spectra in these compounds was examined. The effect of interstitial Mn atoms was found to be crucial for the x-ray magnetic dichroism at the Mn and As K and $L_{2,3}$ edges in the (Ga,Mn)As DMS. The influence of the exchange splitting and spin-orbit coupling strength on each of the constituent atoms were furthermore analyzed. The orientation dependence of the XMCD and XMLD at the Mn $L_{2,3}$ edges in the (Ga,Mn)As DMS was investigated by calculating the XMCD and XMLD spectra for the $\langle 001\rangle$ and $\langle 110\rangle$ magnetization axis. We found a quite small anisotropy in the XMCD and a giant anisotropy in the XMLD at the Mn $L_{2,3}$ edges. The exchange splitting of the initial Mn $2p$ core level was found to be responsible for huge magnetocrystalline anisotropy of the XMLD at the Mn $L_{2,3}$ edges. The calculated results are compared with available experimental data.

DOI: 10.1103/PhysRevB.81.075209 PACS number(s): 75.50.Cc, 71.20.Lp, 71.15.Rf

I. INTRODUCTION

Diluted magnetic semiconductors (DMSs) are semiconductors alloyed with magnetic elements.[1] The physical properties of these materials can be tuned by both charge and spin, thus, they have great potential of being used in a wide variety of spintronic applications, such as magneto-optical, magnetoelectrical, and magnetotransport devices. Spintronics (spin+electronics) is the technology that transforms reading and writing information by spin rather than by electron charge. This field is in-between magnetic and electrical properties of semiconductors. Many researches have been devoted to the study of dilute magnetic semiconductors for use as materials for spintronics.

In this respect Mn-doped III-V semiconductors are among the most frequently studied. In particularly (Ga,Mn)As where the carrier-induced ferromagnetic exchange is well established.[2,3] Mn-doped DMSs are most suitable for spintronic applications since the Mn ion possess the largest magnetic moment compared to other $3d$ transitional metals and it also creates a fully polarized stable state due to its half-filled $3d$ bands. Experimentally, ferromagnetism in (Ga,Mn)As is observed when Mn doping reaches approximately 1% and the system is near the Mott insulator-to-metal transition.[4] At larger Mn concentrations, the localization length of impurity-band states is extended to a degree that allows them to mediate ferromagnetic exchange interaction between Mn moments, even though the moments are dilute. At even higher Mn concentrations, the impurity band gradually merges with the valence band[5] and the impurity states become delocalized. In these metallic (Ga,Mn)As ferromagnets, on which we focus in the following sections, the coupling between Mn local moments is mediated by the p-d kinetic-exchange mechanism.[3]

For the device application, DMSs should satisfy two requirements. The first is carrier controllability and the second is that the Curie temperature (T_C) should be above room temperature. The most widely studied DMS, (Ga,Mn)As, satisfy the first requirement but shows a Curie temperature far below room temperature and therefore appears to be unsuitable for commercial applications. This has led to a considerable world-wide effort in search for new DMSs with higher T_C's.

Dietl *et al.*[6] predicted theoretically that an alloy of $(Ga_{1-x}Mn_x)N$, with an amount of Mn comparable to that used in $(Ga_{1-x}Mn_x)As$, should result in a Curie temperature exceeding room temperature. The prediction led to a flurry of experimental[7–16] and theoretical[17–32] investigations of the (Ga,Mn)N DMS. However, the experimental achievement was not always successful and the experimental data on T_C of (Ga,Mn)N have given a wide range of measured values. (Ga,Mn)N has been reported to be antiferromagnetic,[7] ferromagnetic with T_C around 10 K,[9,15] or ferromagnetic above room temperature.[10–13] The wide variation in reported Curie temperatures suggests that dopant clustering or secondary magnetic phases may be responsible for the observed ferromagnetic signals and indeed the high-temperature ferromagnetism is often attributed to the presence of Mn-rich clusters.[33]

Recently, nitrides and oxides doped with partially filled $4f$ rare-earth (RE) ions have been proposed as an interesting alternative to achieve high T_C in these materials. Ferromagnetism has already been observed in (Ga,Gd)N, with Curie temperature larger than room temperature.[34–36] Furthermore, a colossal magnetic moment of Gd in GaN has been observed, which has a close connection to the observed ferromagnetism in this system.[35] The $4f$ RE elements can have larger magnetic moments than the $3d$ elements, and f electrons can couple strongly with the host s electrons, leading to the possibility of electron-mediated ferromagnetism in these materials.[37] It should be noticed that there is a significant difference in the dopant concentrations needed to induce fer-

romagnetism in GaN between rare earths and the more conventional transition metals such as Mn. In the latter case, concentrations of 3–5 at. % are typically required and this is well above the solid solubility, requiring use of low growth temperatures or nonequilibrium incorporation methods such as ion implantation [$x=1\%$ Mn doping corresponds to $N_{\mathrm{Mn}}=2.2\times10^{20}$ cm^{-3} in (GaMn)As]. By comparison, concentrations of 10^{16}–10^{18} cm^{-3} of Gd and Eu appear sufficient for inducing ferromagnetism and correspondingly large magnetic moments.[38] This has the advantage that there is less compromise in the material quality through the use of lower impurity levels and the material may be codoped with conventional shallow level dopants to control the conductivity. Since the rare-earth dopants may be optically active in these materials, magnetic and optical functionalities on a single chip may be possible.

Despite the partial success, the nature of the host-impurity couplings, and of the ferromagnetic interactions in (Ga,Mn)N, (Ga,Gd)N, and other doped nitrides and oxides, is not very well understood. The accumulated experience of experiments with thin films of magnetically doped semiconductors indicates a high sensitivity of the samples to the technology of their preparation and subsequent heat treatment.[39] The existing technologies, e.g., ion implantation, pulsed laser deposition, reactive magnetic sputtering, etc. permit one to obtain extremely imperfect films in a state far from thermodynamic equilibrium. Those samples, as a rule, are unstable against transition to a nonuniform state, specifically: precipitations of other crystallographic phases, phase separation of the host matrix into insulating and conducting regions, spinodal decomposition in the magnetic subsystem, the appearance of diffusion and implantation profiles, etc. Even in carefully controlled situations, when the precipitation of parasitic phases and aggregations of superparamagnetic clusters with an excess concentration of magnetic ions are prevented as much as possible, it is impossible to completely avoid the fundamental inhomogeneities of DMSs.

Self-consistent band-structure calculations of DMSs have been performed by several authors[17–32,40–52] (see, e.g., review papers of Refs. 2 and 3 for details). Most interest in previous calculations was paid to the nature of the magnetic interactions in the DMSs. In the present study, we focus our attention on x-ray absorption spectra (XAS) as well as x-ray magnetic circular dichroism (XMCD) and x-ray magnetic linear dichroism (XMLD) in (Ga,Mn)As, (Ga,Mn)N, and (Ga,Gd)N DMSs. XMCD experiments measure the difference in the absorption of x-rays with opposite (left and right) directions of circular polarization. The XAS and XMCD at the Ga, Mn, and As K and $L_{2,3}$ edges in the Mn-doped GaAs were measured by several groups.[14,53–68] Takeda *et al.* (Ref. 68) investigated the temperature and magnetic field dependence of soft XMCD at the Mn L_3 edge. The results suggest that the interaction between the substitutional and interstitial $\mathrm{Mn_I}$ ions is antiferromagnetic and that the amount of $\mathrm{Mn_I}$ affects T_C. Angle-dependent XMCD and XMLD at the Mn $L_{2,3}$ edges in (Ga,Mn)As were measured by Edmonds *et al.* (Ref. 62) and Freeman *et al.* (Ref. 63). In contrast to the marginal anisotropy in the XMCD, giant anisotropy in the XMLD was found. Freeman *et al.* (Ref. 63) explain the giant anisotropy in the XMLD using many-electron multiplet calculations in which the $2p$-$3d$ Coulomb and exchange interactions are explicitly taken into account. Kunes and Oppeneer[69] theoretically predicted a large, on the order of the signal itself, anisotropy of the $L_{2,3}$ XMLD in cubic systems such as Fe, Co, and Ni metals. This result was obtained using both *ab initio* band-structure calculations and model calculations in which the $3d$ spin-orbit (SO) interaction was neglected.

Hwang *et al.* in Ref. 14 investigated the electronic structure of Mn-doped GaN using photoemission spectroscopy and XAS. Mn XAS at the L edge have indicated that the Mn ions are in a tetrahedral crystal field and that their valences are 2+. Resonant photoemission spectroscopy has revealed that the main structure of the Mn $3d$ partial density of states (PDOS) appears within the valence band of GaN and as a shoulder above the valence-band maximum of GaN. The XAS and XMCD of the DMS (Ga,Mn)N have been investigated in Refs. 13, 15, 70, and 71. Sarigiannidou *et al.* (Refs. 15 and 70) measured the XAS, XMCD, and XLD spectra at the Ga and Mn K edges. The Mn K XMCD spectrum was found to have a very intense negative peak (1.6% with respect to the step at the edge) in close vicinity to the edge, however, the corresponding XLD spectrum had a very small signal in this energy range. The XAS and XMCD spectra of the (Ga,Mn)N DMS at the Mn $L_{2,3}$ edges were detected by Freeman *et al.* (Ref. 71) and Kevney *et al.* (Ref. 13). Freeman *et al.* in Ref. 71 measured two wurtzite (WZ) and two zinc-blende (ZB) (Ga,Mn)N samples using both fluorescent yield (FY) and total electron yield (TEY) detection methods. For all samples studied, the XMCD L_3 peak was found to be split into two components, a low-energy peak (denoted A) and a higher-energy peak (denoted B), separated by about 0.85 eV. The relative intensities of each peak varied from sample to sample. Zinc-blende samples produced a more pronounce double-peak structure than the wurtzite samples. The measurements obtained in the more surface-sensitive TEY mode showed a larger A/B ratio than measurements in the FY mode. The effect of changing the applied magnetic field on the two peaks in the L_3 region at a constant temperature of 10 K was also investigated. The two components show a different dependence on the applied field: at 0.5 T the two XMCD peaks were of similar magnitude while at 5 T peak A was almost a factor of 2 larger than peak B. The XLD in (Ga,Gd)N at the Ga K and Gd L_3 edges have been measured by Martinez-Criado *et al.* (Ref. 72) and Ney *et al.* (Ref. 73). The XMCD spectra at the Gd L_3 edge were also detected by Ney *et al.* (Ref. 73).

Theoretically dichroism spectra in DMSs were investigated mostly using atomic multiplet calculations with some adjustable parameters.[15,62,63] Density-functional calculations of XMCD at Ga, Mn, and As L_3 and K edges in (Ga,Mn)As have also been reported.[51] The theory describes reasonably well the shape of the XMCD spectra at the Mn, As, and Ga L_3 edges. The Mn, As, and Ga XMCD spectra at the K edges has also been predicted. It appeared later that the predictions were not in perfect agreement with the experiment. In particular, the calculated Mn and As K XMCD spectra showed sharp negative peaks at the onset of the pre-edge, which were not present in the experimental spectra measured by Freeman *et al.* (Ref. 66). Titov *et al.* in Ref. 32 presented

combined experimental and theoretical investigations of the x-ray absorption near-edge structure at the *K* edge of Mn and valence states of Mn in the (Ga,Mn)N DMS. The calculated *K*-edge spectra fit well the experimental data obtained on samples of $(Ga_{1-x}Mn_x)N$ with a wide range of Mn doping (from $x=0.3\%$ to 5.7%). The comparison between the measured spectra and the results of the *ab initio* calculations offered a clear interpretation of the pre-edge structure: it is mainly due to dipolar transitions with a single peak in the case of Mn^{2+} and an additional peak for Mn^{3+}.

The paper is organized as follows. The details of the calculations are described in Sec. II. Section III presents structural models for (Ga,Mn)As, (Ga,Mn)N, and (Ga,Gd)N DMSs used in the present work. Section IV is devoted to the electronic structure as well as XMCD and XMLD properties of the DMSs calculated with the fully relativistic Dirac linear muffin-tin orbital (LMTO) band-structure method. The results are compared with available experimental data. Finally, the results are summarized in Sec. V.

II. COMPUTATIONAL DETAILS

Magneto-optical (MO) effects refer to various changes in the polarization state of light upon interaction with materials possessing a net magnetic moment, including rotation of the plane of linearly polarized light (Faraday, Kerr rotation), and the complementary differential absorption of left and right circularly polarized light (circular dichroism). In the near visible spectral range these effects result from excitation of electrons in the conduction band. Near x-ray absorption edges, or resonances, magneto-optical effects can be enhanced by transitions from well-defined atomic core levels to transition-symmetry-selected valence states.

For a crystal of cubic symmetry, where the magnetization $\mathbf{M}$ is parallel to the z axis, the dielectric tensor is composed of the diagonal ε_{xx} and ε_{zz} and the off-diagonal ε_{xy} components in the form

$$\varepsilon = \begin{pmatrix} \varepsilon_{xx} & \varepsilon_{xy} & 0 \\ -\varepsilon_{xy} & \varepsilon_{xx} & 0 \\ 0 & 0 & \varepsilon_{zz} \end{pmatrix}. \tag{1}$$

A complete description of the MO effects is given by the four nonzero elements of the dielectric tensor or, equivalently, by the complex refractive index $n(\omega)$

$$n(\omega) \equiv \sqrt{\varepsilon(\omega)} = 1 - \delta(\omega) + i\beta(\omega) \tag{2}$$

for several normal modes corresponding to the propagation of pure polarization states along specific directions in the sample, which can be obtained by solving Maxwell's equations.[74] Two of these modes are for circular components of opposite $(\pm)$ helicity with the wave vector $\mathbf{h} \| \mathbf{M}$ and have indices

$$n_\pm = 1 - \delta_\pm + i\beta_\pm = \sqrt{\varepsilon_{xx} \pm i\varepsilon_{xy}}. \tag{3}$$

The other two modes are for linear polarizations with $\mathbf{h} \perp \mathbf{M}$.[75] One has the electric vector $\mathbf{E} \| \mathbf{M}$ and index $n_\| = 1 - \delta_\| + i\beta_\| = \sqrt{\varepsilon_{zz}}$. The other has $\mathbf{E} \perp \mathbf{M}$ and $n_\perp = 1 - \delta_\perp + i\beta_\perp = \sqrt{(\varepsilon_{xx}^2 + \varepsilon_{xy}^2)/\varepsilon_{xx}}$.

X-ray magnetic circular dichroism is given by $\beta_+ - \beta_-$ and is first order in M. Magnetic linear dichroism $n_\perp - n_\|$ (also known as the Voigt effect) is quadratic in M. The Voigt effect is present in both ferromagnets and antiferromagnets while the first-order MO effects in the forward scattering beam are absent with the net magnetization in antiferromagnets.

Within the one-particle approximation, the absorption coefficient $\mu_j^\lambda(\omega)$ for incident x-ray of polarization λ and photon energy $\hbar\omega$ can be determined as the probability of electronic transitions from initial core states with the total angular momentum j to final unoccupied Bloch states

$$\mu_\lambda^j(\omega) = \sum_{m_j} \sum_{n\mathbf{k}} |\langle \Psi_{n\mathbf{k}} | \Pi_\lambda | \Psi_{jm_j} \rangle|^2 \delta(E_{n\mathbf{k}} - E_{jm_j} - \hbar\omega) \times \theta(E_{n\mathbf{k}} - E_F), \tag{4}$$

where Ψ_{jm_j} and E_{jm_j} are the wave function and the energy of a core state with the projection of the total angular momentum m_j; $\Psi_{n\mathbf{k}}$ and $E_{n\mathbf{k}}$ are the wave function and the energy of a valence state in the nth band with the wave vector $\mathbf{k}$; and E_F is the Fermi energy.

Π_λ is the electron-photon interaction operator in the dipole approximation

$$\Pi_\lambda = -e\boldsymbol{\alpha}\mathbf{a}_\lambda, \tag{5}$$

where $\boldsymbol{\alpha}$ are the Dirac matrices, $\mathbf{a}_\lambda$ is the λ polarization unit vector of the photon vector potential, with $a_\pm = 1/\sqrt{2}(1, \pm i, 0)$, $a_\| = (0,0,1)$. Here, + and − denotes, respectively, left and right circular photon polarizations with respect to the magnetization direction in the solid. Then, x-ray magnetic circular and linear dichroisms are given by $\mu_+ - \mu_-$ and $\mu_\| - (\mu_+ + \mu_-)/2$, respectively. More detailed expressions of the matrix elements for the spin-polarized fully relativistic LMTO method may be found in Refs. 76 and 77.

Usually, the exchange splitting of a core shell is small compared to the band width of final valence states and can be neglected. However, the exchange splitting of the $2p_{1/2,3/2}$ states of $3d$ transition metals may be as large as 0.4 eV. Then, the transitions from the core states with different m_j in Eq. (4) occur at different photon frequencies. This may lead to the appearance of giant XMLD in cubic $3d$ metals and its strong dependence on the magnetization direction.[69]

All the calculations presented in this work were performed using the spin-polarized fully relativistic LMTO method[78,79] for the experimentally observed lattice constants: $a=5.654$ Å for GaAs,[80] $a=3.189$ Å and $c=5.185$ Å for wurtzite-type GaN, and $a=4.500$ Å for zinc-blende-type GaN.[81] We used the Perdew-Wang[82] parameterization of the exchange-correlation potential. Brillouin zone (BZ) integrations were performed using the improved tetrahedron method[83] and charge self-consistently was obtained on a grid of 84 $\mathbf{k}$ points in the irreducible part of the BZ of $(Ga_{1-x}Mn_x)As$ $(x=0.03)$. For wurtzite-type $(Ga_{1-x}Mn_x)N$ and $(Ga_{1-x}Gd_x)N$ we used a grid of 193 $\mathbf{k}$ points in the irreducible part of the BZ. To improve the potential we included additional interstitial spheres. The basis consisted of Mn, Ga, and As s, p, and d; Gd s, p, d, and f; and N s and p LMTOs.

X-ray absorption and dichroism spectra were calculated taking into account the exchange splitting of core levels. The finite lifetime of a core hole was accounted for by folding the spectra with a Lorentzian. The widths of K, L_2, and L_3 core-level spectra: $\Gamma_K=1.11$ eV, $\Gamma_{L_2}=0.97$ eV, and $\Gamma_{L_3}=0.36$ eV for Mn; $\Gamma_K=1.76$ eV, $\Gamma_{L_2}=0.77$ eV, and $\Gamma_{L_3}=0.77$ eV for Ga; $\Gamma_K=2.09$ eV, $\Gamma_{L_2}=0.95$ eV, and $\Gamma_{L_3}=0.94$ eV for As; $\Gamma_{L_2}=3.87$ eV and $\Gamma_{L_3}=3.72$ eV for Gd; and $\Gamma_K=0.5$ eV for N were taken from Ref. 84. The finite apparative resolution of the spectrometer was accounted for by a Gaussian of width 0.6 eV.

Strong electronic correlations in Mn $3d$ and Gd $4f$ shells were treated at the mean-field level using the LSDA+U approach[85] in its rotationally invariant implementation which is describe in details in our previous paper.[86] The effective on-site Coulomb repulsion U was treated as an adjustable parameter. We used $U=4$ eV for the Mn $3d$ states in (Ga,Mn)As and $U=7$ eV for the Gd $4f$ states in (Ga,Gd)N DMS. The exchange integral J was estimated from constrained local spin-density approximation (LSDA) calculations and values of 1.0 and 0.68 eV were used for the Mn and Gd states, respectively.

III. STRUCTURAL MODEL

GaAs crystallizes in the zinc-blende-type crystal structure with the $F\bar{4}3m$ (No. 216) space group. Ga and As ions occupy the $4a$ ($x=0$, $y=0$, $z=0$) and $4c$ ($x=\frac{1}{4}$, $y=\frac{1}{4}$, $z=\frac{1}{4}$) Wyckoff positions, respectively. The elements in the (Ga,Mn)As compound have nominal atomic structures $[\mathrm{Ar}]3d^{10}4s^24p^1$ for Ga, $[\mathrm{Ar}]3d^54s^2$ for Mn, and $[\mathrm{Ar}]3d^{10}4s^24p^3$ for As. This circumstance correctly suggests that the most stable and therefore most common position of Mn in the GaAs host lattice is on the Ga site where its two $4s$ electrons can participate in crystal bonding in much the same way as the two Ga $4s$ electrons.[3]

A significant fraction of the Mn ions in (Ga,Mn)As DMSs is also incorporated into interstitial positions.[87,88] Direct experimental evidence for Mn impurities occupying interstitial ($\mathrm{Mn_I}$) rather than substitutional positions was uncovered by combined channeling Rutherford backscattering and particle-induced x-ray emission measurements[87] as well as by scanning tunneling microscopy.[88–91] In highly doped as-grown samples, the experiment identified nearly 20% of Mn as residing on interstitial positions. Adsorption pathways that can funnel Mn to interstitial sites were identified theoretically using *ab initio* calculations of the potential-energy surface of Mn adsorbed on GaAs(001).[42] First-principles calculations have also confirmed that interstitial $\mathrm{Mn_I}$ impurities in GaAs are metastable, showing that the three distinct positions they can occupy are two tetrahedral T positions surrounded by four nearest-neighbor As or Ga atoms ($\mathrm{As_4}$ or $\mathrm{Ga_4}$), and one hexagonal position with three Ga and three As nearest neighbors. Among the three interstitial sites the hexagonal position is clearly less favorable, especially so in an overall p-type (Ga,Mn)As material.[92] The typical energy barrier for Mn diffusion between interstitial sites is approximately 1 eV.[49,92] On the other hand, diffusion of Mn between Ga substitutional positions involves a kick-out mechanism of $\mathrm{Mn_I}+\mathrm{Ga_{Ga}}\rightarrow\mathrm{Mn_{Ga}}+\mathrm{Ga_I}$ for which the typical barrier is about 3 eV.[42] Interstitial $\mathrm{Mn_I}$ is therefore much more mobile than substitutional $\mathrm{Mn_{Ga}}$.

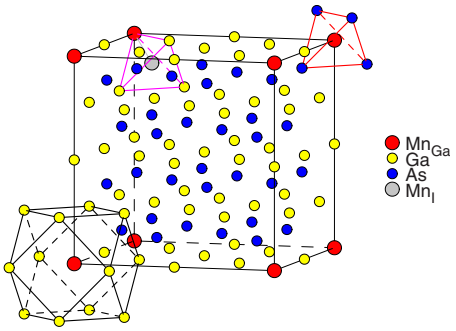

FIG. 1. (Color online) Schematic representation of the $(\mathrm{Ga_{1-x}Mn_x})\mathrm{As}$ structure with one substitutional $\mathrm{Mn_{Ga}}$ and one interstitial $\mathrm{Mn_I}$ atom in the unit cell ($x=0.06$). The interstitial $\mathrm{Mn_I}$ atom is shown in the $\mathrm{Mn_1Ga_3}$ position (see the explanation in the text).

The calculations of the electronic structure and XMCD in $(\mathrm{Ga_{1-x}Mn_x})\mathrm{As}$ DMSs were performed for a $2a\times2a\times2a$ supercells of the cubic GaAs unit cell with one of the Ga ions replaced by Mn. The compositions with $x=0.03125$ (1/32), 0.0625 (1/16), and 0.125 (1/8) were obtained by using a simple cubic $P\bar{4}3m$ (No. 215), bcc $I\bar{4}3m$ (No. 217), and fcc $F\bar{4}3m$ (No. 216) unit cells, respectively. We investigated also the influence of an interstitial $\mathrm{Mn_I}$ impurity on the electronic structure and XMCD spectra by placing an additional Mn ion in one of the tetrahedral T positions of the simple cubic 64-atom (Ga,Mn)As unit cell. This corresponds to an effective Mn content of $x=0.06$ with an equal number of substitutional $\mathrm{Mn_{Ga}}$ and interstitial $\mathrm{Mn_I}$ ions. The calculations were performed for three different positions of $\mathrm{Mn_I}$, in which the interstitial Mn ion was surrounded by a tetrahedron formed by $\mathrm{Mn_{Ga}}$ and three Ga ions ($\mathrm{Mn_1Ga_3}$), four As ions ($\mathrm{As_4}$), or four Ga ions ($\mathrm{Ga_4}$), with the distances between the substitutional and interstitial Mn ions being 2.448, 4.897, and 7.345 Å, respectively. The positions of a substitutional $\mathrm{Mn_{Ga}}$ and interstitial $\mathrm{Mn_I}$ ions in $(\mathrm{Ga_{1-x}Mn_x})\mathrm{As}$ with $x=0.06$ are illustrated in Fig. 1 for a 64-atom GaAs unit cell. Each $\mathrm{Mn_{Ga}}$ ion is surrounded by a tetrahedron of four As nearest neighbors ($\mathrm{As_1}$) at the same distance of 2.448 Å. The second coordination sphere consists of 12 Ga atoms ($\mathrm{Ga_2}$) at the distance of 3.998 Å.

GaN exists in two crystallographic modifications, namely, WZ, with space group $P6_3/mc$ (No. 186) (Ga ions occupy the $2b$ positions $x=\frac{1}{3}$, $y=\frac{2}{3}$, and $z=0$, and N ions are placed at the $2b$ sites $x=\frac{1}{3}$, $y=\frac{2}{3}$, and $z=0.377$) and ZB type, with space group $F\bar{4}3m$ (No. 216).[81,93] Although the two structures have different space groups, they are in fact very similar.[93,94] They have the same local tetrahedral environment and start to differ only in their third-nearest-neighbor atomic arrangement. The cubic phase is described by its lattice constant a_{ZB}. The WZ structure can be characterized by three structural parameters: a_{WZ}, c_{WZ}, and u_{WZ}. In an ideal wurtzite structure, one finds $a_{\mathrm{WZ}}=a_{\mathrm{ZB}}/\sqrt{2}$, $(c/a)_{\mathrm{WZ}}=\sqrt{8/3}$,

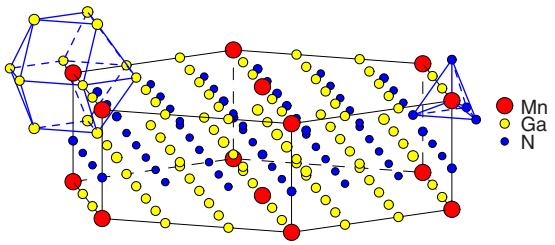

FIG. 2. (Color online) Schematic representation of the $(Ga_{1-x}Mn_x)N$ structure for $x=0.06$ (see text).

and the internal structure parameter $u_{WZ}=0.375$. For the real wurtzite compound such as GaN, due to the lower crystal symmetry, the N positional parameter $u_{WZ}^{GaN}=0.377$ differs from these ideal values.

The calculations of the electronic structure of the $(Ga_{1-x}Mn_x)N$ and $(Ga_{1-x}Gd_x)N$ DMSs were performed for a $3a\times3a\times1c$ supercells of the wurtzite-type GaN unit cell with one of the Ga ions replaced by Mn or Gd. The supercell calculations were performed for the composition $x=0.0556(1/18)$, using the simple trigonal $P3m1$ (No. 156) space group. For (Ga,Mn)N and (Ga,Gd)N in the zinc-blende-type crystal structure we perform the calculations for the $x=0.03125$ using the same supercells as used for the (Ga,Mn)As calculations. The substitutional $(Ga_{1-x}Mn_x)N$ positions are illustrated in Fig. 2 for a 36-atom GaAs unit cell containing one substitutional Mn_{Ga} atom ($x=0.0556$). The Mn_{Ga} (Gd_{Ga}) atom has four N nearest neighbors: three N atoms at the distance of 1.949 Å and one N atom at 1.955 Å. The second-neighbor shell consists of 12 Ga atoms: six at 3.180 Å and six at 3.189 Å.

In the (Ga,Mn)As DMSs, interstitial Mn strongly affects the Curie temperature T_C, however, the importance of defects and their positions depend very much on the host compound. The significantly smaller volume of GaN than GaAs leaves little room for Mn (Gd) interstitials whereas the larger atomic size of As greatly hinders the formation of As split interstitials. The results of Keavney *et al.*[13] suggest that the interstitial Mn does not exist in significant quantities in their (G,Mn)N samples.

IV. RESULTS AND DISCUSSION

A. (Ga,Mn)As DMS

1. Energy band structure

Figure 3 presents total and partial DOS calculated within LSDA for the 64-atom unit cell of $(Ga_{1-x}Mn_x)As$ with $x=0.03$, i.e., an experimentally accessible Mn concentration. From the figure it is clear that $(Ga_{1-x}Mn_x)As$ has the electronic structure of a half-metal. This result is largely confirmed by all density-functional calculations to date using the LSDA approach.[18,95–97] Because of the low Mn content, the densities of Ga and As states, except for the nearest As_1 and next-nearest Ga_2 neighbors of the Mn impurity, are similar to those calculated for GaAs with the same interatomic distances. The Mn d states are split by the on-site exchange interaction into almost completely filled majority-spin and

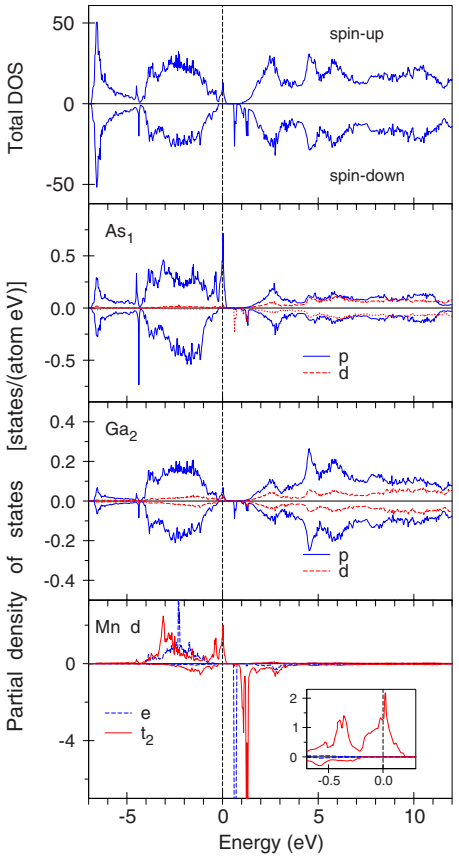

FIG. 3. (Color online) The LSDA total [in states/(cell eV)] and partial [in states/(atom eV)] densities of states for the substituted Mn_{Ga} ion and for its first As_1 and second Ga_2 nearest neighbors in $Ga_{1-x}Mn_xAs$ ($x=0.03$). The inset is a blowup of the PDOS of Mn close to the Fermi energy. The Fermi energy is at zero.

unoccupied minority-spin states. The crystal field at the Mn site (T_d point symmetry) causes the splitting of d orbitals into a doublet e ($3z^2-1$ and x^2-y^2) and a triplet t_2 (xy, yz, and xz). The majority spin Mn e states are completely filled and show a sharp DOS peak at −2.4 eV. The Mn t_2 states hybridize much stronger with the As p states. The corresponding bonding states span the energy range from −4 to −1.5 eV whereas the antibonding ones form two DOS peaks just below and exactly at the Fermi level. Although the dominant contribution to the bands responsible for these DOS peaks is provided by the majority-spin Mn t_2 states and p states of four nearest As_1 ions, the weight of more distant Ga and As ions in the corresponding wave functions is also substantial. The unoccupied minority spin Mn e states form almost flat bands at the very bottom of the conduction band and hybridize weakly with As and Ga states. Bands formed by the minority spin Mn t_2 states cross the bottom of the conduction band and produce a double-peak DOS structure at ~1.2 eV. The strong hybridization of the t_2 states with the As and Ga p states is evidenced by a relatively high contribution of the minority-spin t_2 states to the occupied part of the valence band. The spin splitting of the Ga and As p states is quite small.

Thus, according to the LSDA results, a Mn ion substituted for Ga creates one hole in the majority-spin bands while the

filling of the minority-spin bands does not change. Because of the hole, the spin magnetic moment per (Ga,Mn)As unit cell is reduced from $5\mu_B(S=5/2)$, expected for a Mn^{2+} ion with the completely spin-polarized d shell, to $4\mu_B$ and remains the same up to a Mn content of $x=0.125$. The integer value of the magnetic moment is consistent with the half-metalicity seen in the DOS (Fig. 3). However, the magnetic moment of $4\mu_B$ appears to be smaller than the moment of $\sim 4.4\mu_B$ found experimentally.[58,59,61] Our band-structure calculations produce a spin magnetic moment of $3.751\mu_B$ at the Mn_{Ga} in $(Ga_{1-x}Mn_x)As$ $(x=0.03)$. The population of the majority- and minority-spin Mn d states is 4.467 and 0.836 electronic charges, respectively. The spin magnetic moment of $-0.013\mu_B$ induced at the first neighbor As_1 sites is antiparallel to that of Mn. Twelve Ga_2 ions forming the second-neighbor shell are polarized ferromagnetically with a spin magnetic moment of $0.012\mu_B$ per Ga. The orbital magnetic moment at the Mn_{Ga} site is equal to $0.048\mu_B$. The orbital moments at the Ga and As sites are quite small with the largest one at the As first neighbor sites $(-0.008\mu_B)$.

It is well known that at high hole densities, Mn has a tendency to autocompensate the magnetic moment by occupying donor interstitial sites.[49,92] We investigated the influence of an interstitial Mn_I impurity on the electronic structure and magnetic dichroism by placing it in one of three tetrahedral T positions, surrounded by a Mn_{Ga} atom and three Ga atoms (Mn_1Ga_3), four As atoms (As_4), or four Ga atoms (Ga_4), of the 64-atom (Ga,Mn)As unit cell containing one substitutional Mn_{Ga}. From total energy calculations we found that the energy is the lowest when the interstitial Mn ion occupies the Mn_1Ga_3 tetrahedral position closest to the substitutional Mn_{Ga} and its moment is antiparallel to the Mn_{Ga} moment. This is consistent with the experimental measurements of Edmonds *et al.* (Ref. 59) which present direct evidence for antiferromagnetic coupling between interstitial and substitutional Mn in unannealed (Ga,Mn)As. The Mn $L_{2,3}$ x-ray absorption line shapes display no sizeable site or concentration dependence but in unannealed (Ga,Mn)As the XMCD signal is significantly smaller and increases linearly under high magnetic fields. In contrast, in carefully prepared and annealed (Ga,Mn)As samples a large dichroism signal was found, revealing large magnetic moments per Mn atom and showing that most of the Mn moments are aligned ferromagnetically. Before annealing, the XMCD is smaller and weakly field dependent, demonstrating that a significant fraction of Mn moments are antiferromagnetically coupled. Recently, Takeda *et al.* (Ref. 68) have investigated the temperature and magnetic field dependence of soft x-ray magnetic circular dichroism at the Mn L_3 edge. The results suggest that the interaction between the substitutional and interstitial Mn_I ions is antiferromagnetic and that the amount of Mn_I affects T_C.

Figure 4 presents LSDA densities of d states of the antiferromagnetically coupled substitutional Mn_{Ga} and interstitial Mn_I ions in a 64-atom GaAs unit cell $(x=0.06)$. In order to demonstrate more clearly the effect of the Mn d-(Ga, As) pd hybridization the densities of the p and d states of As and Ga ions nearest to Mn_{Ga} and Mn_I (As_1 and Ga_1, respectively) are also shown. In the presence of Mn_I the point symmetry of both the Mn_{Ga} and Mn_I sites lowers to C_{3v}, which causes

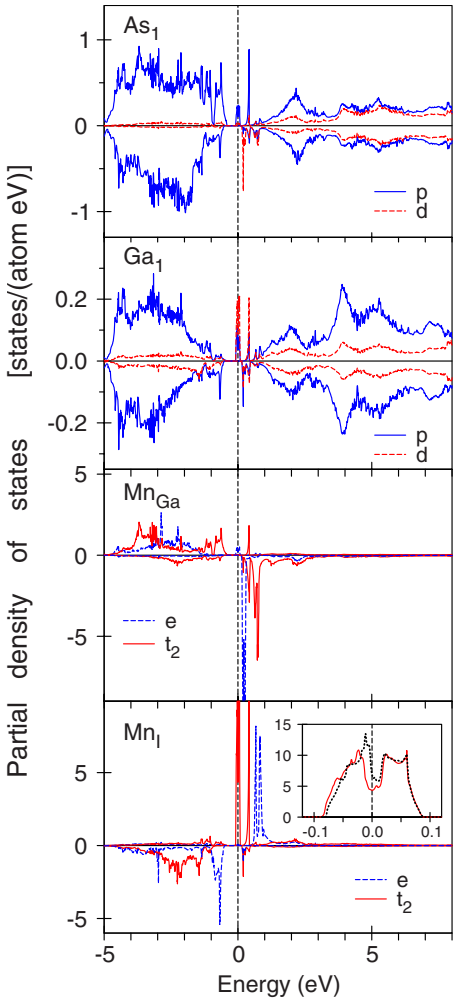

FIG. 4. (Color online) The partial density of states [in states/(atom eV)] of $Ga_{1-x}Mn_xAs$ $(x=0.06)$ for the substituted Mn_{Ga} atom, interstitial Mn_I and their first-nearest neighbors (As_1 and Ga_1, respectively) in the LSDA. The inset is a blowup of the PDOS of Mn_I close to the Fermi energy for not optimized (full line) and optimized (dotted line) crystal structures. The Fermi energy is at zero.

additional splitting of the Mn t_2 states into a singlet a_1 and a doublet e'. The sum of the DOS projected onto the a_1 and e' states is denoted as t_2 in Fig. 4. An interstitial Mn ion acts as a donor of two s electrons. When, as in the (Ga,Mn)As unit cell described above, the concentrations of the substitutional and interstitial Mn impurities are equal, one of the electrons fills the majority-spin hole in the valence band. Figure 4 shows that the second electron starts to fill the narrow bands formed by the majority-spin d states of the Mn_I ion which lie just below the minority-spin Mn_{Ga} d bands. As a consequence, the DOS peak formed exactly at ε_F by strongly hybridized majority-spin Mn_{Ga} d and As p states (see Fig. 3), becomes occupied. The Fermi level shifts upward by ~ 0.6 eV from its position at the top of the valence band in the calculation with a single substitutional Mn_{Ga} impurity and crosses the very bottom of the GaAs conduction bands. The majority-spin Mn_I t_2 states are split into two peaks because of the hybridization with Mn_{Ga} states via the p states of the nearest As and Ga neighbors. There is a quite strong peak

of the majority-spin Mn_I t_2 states in the −0.1 to 0.1 eV energy range, however, the Fermi level is situated in a local minimum of the DOS (see the inset at the bottom panel of Fig. 4). Another narrow peak of the majority-spin Mn_I d states of t_2 symmetry is situated around 0.4 eV above the Fermi energy. The Mn_I majority d double peak of e symmetry is situated in the 0.6–0.9 eV energy range above the Fermi energy. The Mn_I minority band has almost no d character above ε_F.

The Fermi level is situated at a strong PDOS peak of Mn_I t_2 symmetry (Fig. 4). This may imply a structural instability and a lattice distortion which can be induced by it. To investigate possible lattice distortion we optimized the position of the interstitial Mn_I and the positions of its neighbor atoms (M_{Ga} and three Ga atoms) with fixed positions of the other atoms using the VASP-SGGA method.[98–100] We found only minor influence of the structure relaxation on the partial DOS in close vicinity of the Fermi level (± 0.1 eV), further away from the Fermi level the PDOSs did not change. The results are shown in the inset at the bottom panel of Fig. 4 (dotted line). Similar results were obtained during the relaxation of the whole (Ga,Mn)As crystal structure (we adjusted the value of the lattice constant and the positions of all the 64 atoms in the unit cell). The lattice optimization also did not affect the XAS and XMCD spectra which are extended in a wide energy interval.

The magnetic moment per (Ga,Mn)As unit cell with an additional Mn_I atom is strongly reduced to $0.994\mu_B$ due to the antiparallel alignment of the Mn_I and Mn_{Ga} moments. It should be noticed that in the calculations presented in Fig. 4 an equal number of substitutional and interstitial Mn ions is assumed, which strongly overestimates the typical experimental situation.[3] For a more realistic ratio of Mn_I to Mn_{Ga} concentrations one would expect a much weaker compensation of the Mn_{Ga} spin moment by Mn_I and a smaller shift of the Fermi level. Experimentally, an apparent "magnetization deficit" of more than 50% (i.e., $\mu \leq 2.5\mu_B/\mathrm{Mn}$) has been observed using superconducting quantum interference device magnetometry.[4] Understanding and minimizing this effect is vital since incomplete participation in the ferromagnetism will limit the Curie temperature.

2. XMCD spectra at the $L_{2,3}$ edges

X-ray absorption spectra and x-ray magnetic circular dichroism at the $L_{2,3}$ edges of impurity Mn ions in (Ga,Mn)As DMS were measured by several groups.[54,55,57–60,62–68] Figures 5(a) and 5(b) present experimental XAS and XMCD spectra[57] of (Ga,Mn)As at the Mn $L_{2,3}$ edges together with the spectra calculated in the LSDA. The theory reproduces reasonably well the experimental Mn $L_{2,3}$ XAS. The main maximum of the Mn L_3 XAS can be attributed to the transitions from $2p$ core level to the empty minority-spin d states of e symmetry. A high-energy shoulder shifted upward by about 1 eV with respect to the main maximum is from the $2p \rightarrow t_2$ transitions. The next high-energy shoulder at around 640.5 eV reflects the corresponding peak in the Mn d DOS arising from the Mn d-As p hybridization. The experimental Mn XAS has a double-peak structure at the L_2 edge with almost equal intensity. The theory also produces a two-peak

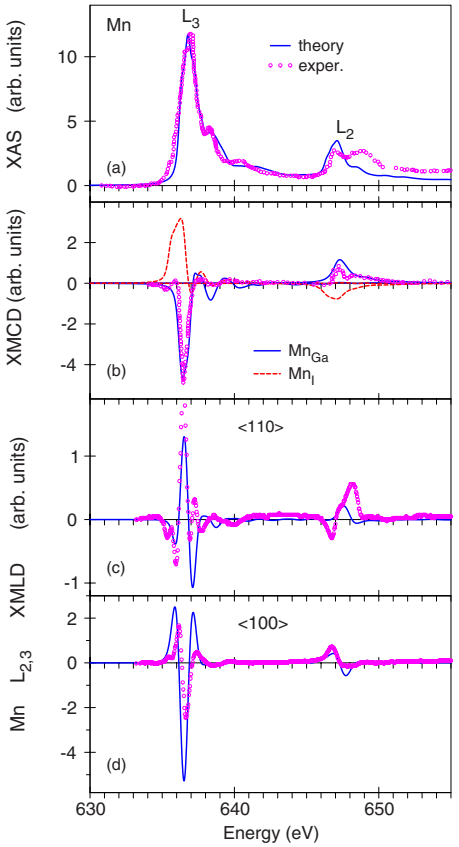

FIG. 5. (Color online) (a) X-ray absorption and (b) XMCD experimental spectra (Ref. 57) (circles) of (Ga,Mn)As (x=0.07) at the Mn $L_{2,3}$ edges and theoretically calculated spectra for the substituted Mn_{Ga} (full line) and interstitial Mn_I (dashed lines) sites (for x=0.06); (c) theoretically calculated (full line) and experimentally measured (Ref. 63) (circles) XMLD spectra for **E** along ⟨110⟩ direction; and (d) theoretically calculated (full line) and experimentally measured (Ref. 63) (circles) XMLD spectra for **E** along ⟨100⟩ direction.

structure but with smaller intensity for the high-energy peak. Both the L_2 and L_3 XAS reflects the energy distribution of empty Mn d states but it is not clear why Mn L_2 and L_3 XASs have so different shapes.

The LSDA calculations reproduce all fine structures of the experimental Mn $L_{2,3}$ XMCD spectra quite well except for the low-energy positive peak at around 636 eV [Fig. 5(b)]. This structure is due to transitions from the $2p$ core level to partially filled majority-spin Mn_I d states of the t_2 symmetry situated at the Fermi level (see Fig. 4). The theory strongly overestimates the intensity of the peak. It may be explain by the fact that the calculations presented in Fig. 5 have been done for a 50% concentration of the interstitial Mn_I atoms while the typical concentration of the interstitial Mn atoms is usually at least ten times smaller.[3] One would expect strong suppression of the peak with smaller Mn_I concentration. The shapes of the Mn_{Ga} XMCD spectra at the $L_{2,3}$ edges with and without additional interstitial Mn_I ion are almost the same.

Angle-dependent x-ray magnetic Mn $L_{2,3}$ circular and linear dichroism from (Ga,Mn)As were measured by Edmonds *et al.* (Ref. 62) and Freeman *et al.* (Ref. 63), respectively. In contrast to a marginal anisotropy in the XMCD, giant aniso-

TABLE I. Squared angular matrix elements $\Omega_\perp^2$ and $\Omega_\parallel^2$ (multiplied by 90) for dipole allowed transitions at the L_2 edge from initial core states with different projections m_j of the total angular momentum $j=1/2$ to majority- and minority-spin d cubic harmonics.

	$\Omega_\perp^2$			$\Omega_\parallel^2$		
	$-\frac{1}{2}$	$\frac{1}{2}$	Σ_{m_j}	$-\frac{1}{2}$	$\frac{1}{2}$	Σ_{m_j}
$d^\uparrow_{yz}$	3	0	3	0	6	6
$d^\uparrow_{zx}$	3	0	3	0	6	6
$d^\uparrow_{xy}$	0	6	6	0	0	0
Σ_{t_2}	6	6	12	0	12	12
$d^\uparrow_{3z^2-1}$	0	2	2	8	0	8
$d^\uparrow_{x^2-y^2}$	0	6	6	0	0	0
Σ_e	0	8	8	8	0	8
$d^\downarrow_{yz}$	0	3	3	6	0	6
$d^\downarrow_{zx}$	0	3	3	6	0	6
$d^\downarrow_{xy}$	6	0	6	0	0	0
Σ_{t_2}	6	6	12	12	0	12
$d^\downarrow_{3z^2-1}$	2	0	2	0	8	8
$d^\downarrow_{x^2-y^2}$	6	0	6	0	0	0
Σ_e	8	0	8	0	8	8

tropy in the linear dichroism was found. We also found very small anisotropy for the x-ray magnetic circular dichroism at the Mn $L_{2,3}$ edges. The anisotropy in the linear dichroism appears to be even larger than experimentally observed [see Figs. 5(c) and 5(d)]. Neither the magnitude nor the strong angular dependence of the calculated XMLD spectra is affected if the SO coupling strength is set to zero for all valence states. If, however, the exchange splitting of the Mn $2p_{1/2,3/2}$ core states is neglected, the magnitude of the XMLD becomes 30 times smaller but the spectra still exhibit strong dependence on the magnetization direction. When, additionally, the SO coupling of the valence states is switched off, the linear dichroism disappears completely. In contrast to XMLD, the magnitude of the calculated Mn $L_{2,3}$ XMCD spectra is not affected by the splitting of the Mn $2p_{1/2,3/2}$ states, although their spectral shape changes somewhat when the splitting is not taken into account.

Qualitative understanding of the huge magnetic linear dichroism at the Mn $L_{2,3}$ edges is provided by an analysis of the matrix elements for transitions from the SO split $2p_{1/2}$ and $2p_{3/2}$ states to the spin- and crystal-field split $3d$ states. XMLD is proportional to the difference in the absorption coefficients $\mu_\parallel$ and $\mu_\perp$ for x-rays with the polarization parallel and perpendicular to the magnetization direction. The x-ray transition-matrix elements obey the dipolar selection rules on the angular momentum quantum numbers j, m_j of the initial and final states such that $\Delta m_j = \pm 1$ or $\Delta m_j = 0$ and $\Delta j = 0, \pm 1$. To $\mu_\pm$ only transitions with $\Delta m_j = \pm 1$ contribute whereas to $\mu_\parallel$ only $\Delta m_j = 0$ transitions contribute. The XMLD is thus the intensity difference between the resonant transitions with $\Delta m_j = 0$ and the averaged $\Delta m_j = \pm 1$ transitions whereas the XMCD relates to the difference between the $\Delta m_j = +1$ and $\Delta m_j = -1$ transitions.

Tables I and II present squared angular-matrix elements $\Omega_\parallel^2$ and $\Omega_\perp^2 = (\Omega_+^2 + \Omega_-^2)/2$ for dipole-allowed transitions from $|jm_j\rangle$ core states with different projection of the total angular momentum m_j to majority- and minority-spin d cubic harmonics at the L_2 and L_3 edges, respectively. Although the spin-dependent part $V_{\rm sp}$ of the exchange-correlation potential mixes core states with $j = l \pm 1/2$ and j is no longer a good quantum number, the admixture of the m_j state with $j' = 2l - j$ to the core wave function of a $2p$ state of a transition-metal ion is very weak and is neglected here. It is easy to see that each pair of initial and final states gives a nonzero contribution $\Omega_\parallel^2 - \Omega_\perp^2$ to the linear dichroism. Moreover, the sum of the probabilities of transitions from an initial state with a given m_j to degenerate t_2 (d_{xy}, d_{yz}, and d_{zx}) and e (d_{3z^2-1} and $d_{x^2-y^2}$) final states, denoted in Tables I and II as Σ_{t_2} and Σ_e, still produces strong linear dichroism, with the contributions of the transitions to e and t_2 states being of opposite signs. The probabilities to absorb photons with $\mathbf{E} \parallel \mathbf{M}$ and $\mathbf{E} \perp \mathbf{M}$ become equal, only when the initial core states are degenerate and the sum over m_j is taken.

In (Ga,Mn)As, however, the exchange splitting within the Mn $2p_{1/2}$ and $2p_{3/2}$ subshells is about 0.4 eV, which is larger than the widths of unoccupied minority-spin e($\sim$0.15 eV) and t_2($\sim$0.2 eV) states (see Fig. 3). Transitions from each $|jm_j\rangle$ core state to the e and t_2 states produce two XMLD peaks of opposite signs. The sum of these two-peak contributions, shifted by $\sim$0.4 eV each, gives the XMLD spectrum shown in Fig. 5(a). If the splitting of the Mn $2p_{1/2,3/2}$ states is neglected, the contributions to XMLD coming from initial states with different m_j cancel each other and much weaker calculated XMLD appears because of the lifting of the degeneracy of the e and t_2 states by the SO interaction. The strong dependence of the Mn $L_{2,3}$ XMLD on the magnetization direction can be explained by taking into account the transformations of the d cubic harmonics to a new frame with $z' \parallel \mathbf{M}$ as was shown in Ref. 69. The XMLD is proportional to a combination of individual partial densities of

TABLE II. Squared angular matrix elements $\Omega_{\perp}^2$ and $\Omega_{\parallel}^2$ (multiplied by 90) for dipole allowed transitions at the L_3 edge from initial core states with different projections m_j of the total angular momentum $j=3/2$ to majority- and minority-spin d cubic harmonics.

	$\Omega_{\perp}^2$					$\Omega_{\parallel}^2$				
$\|f\rangle$	$-\frac{3}{2}$	$-\frac{1}{2}$	$\frac{1}{2}$	$\frac{3}{2}$	Σ_{m_j}	$-\frac{3}{2}$	$-\frac{1}{2}$	$\frac{1}{2}$	$\frac{3}{2}$	Σ_{m_j}
$d_{yz}^{\uparrow}$	0	6	0	0	6	9	0	3	0	12
$d_{zx}^{\uparrow}$	0	6	0	0	6	9	0	3	0	12
$d_{xy}^{\uparrow}$	9	0	3	0	12	0	0	0	0	0
Σ_{t_2}	9	12	3	0	24	18	0	6	0	24
$d_{3z^2-1}^{\uparrow}$	3	0	1	0	4	0	16	0	0	16
$d_{x^2-y^2}^{\uparrow}$	9	0	3	0	12	0	0	0	0	0
Σ_e	12	0	4	0	16	0	16	0	0	16
$d_{yz}^{\downarrow}$	0	0	6	0	6	0	3	0	9	12
$d_{zx}^{\downarrow}$	0	0	6	0	6	0	3	0	9	12
$d_{xy}^{\downarrow}$	0	3	0	9	12	0	0	0	0	0
Σ_{t_2}	0	3	12	9	24	0	6	0	18	24
$d_{3z^2-1}^{\downarrow}$	0	1	0	3	4	0	0	16	0	16
$d_{x^2-y^2}^{\downarrow}$	0	3	0	9	12	0	0	0	0	0
Σ_e	0	4	0	12	16	0	0	16	0	16

states, which is not invariant under a change in the quantization axis. Consequently, the XMLD anisotropy exists already when the valence-band spin-orbit coupling is neglected. On the other hand, the XAS and XMCD are proportional to the traces of the d density matrices,[69] therefore they are isotropic with regard to the orientation of the magnetization to the crystallographic axes.

Finally, if, as in (Ga,Mn)N DMS with the wurtzite structure, the degeneracy of the Mn e and t_2 states is lifted due to lowering of crystal symmetry, contributions to linear dichroism from transitions to individual d states do not cancel each other even after summation over m_j, $[\Sigma_{m_j}(\Omega_{\perp}^2-\Omega_{\parallel}^2)\neq 0$ in Tables I and II]. In this case strong XLD at the $L_{2,3}$ edges can be observed even for a nonmagnetic $3d$ impurity.

The XAS and XMCD spectra in the (Ga,Mn)As DMS at the As L_3 and Ga $L_{2,3}$ edges were measured by Keavney *et al.* (Ref. 57). From the signs of the L_3 XMCD lowest-energy features the authors concluded that Ga spin magnetic moment is antiparallel to that of the As and parallel to Mn. This is in agreement with our band-structure calculations. The As atoms occupy the first neighbor positions around substituted Mn_{Ga}. On the other hand, the interstitial Mn_I atoms are situated preferably at the Mn_1Ga_3 tetrahedral positions with one Mn_{Ga} and three Ga atoms as the first neighbors. For this reason one would expect less influence of the interstitial Mn_I atoms on the As XMCD spectra than on the Ga ones. Indeed, as may be seen in Fig. 6, the calculation for a 64-atom GaAs unit cell containing only one Mn_{Ga} substitution reproduces quite well the XAS and XMCD spectra. There is only a small disagreement in the relative intensities of the first and the second low-energy peaks of the XAS and in the energy position of the XMCD high-energy peaks in the 1329–1332 eV energy range.

Figure 7 presents theoretical and experimental XAS and XMCD spectra at the Ga L_3 edge. The theoretically calculated XAS spectrum with only one Mn_{Ga} atom in the 64-atom GaAs unit cell (full line) agrees well with the experimental measurements.[57] For the Ga L_3 XMCD spectrum the calculation without the interstitial Mn_I ion reproduces reasonably well low-energy positive structure at 1115 eV but underestimates the intensity of the second negative peak at around 1116 eV. The incorporation in the theory the Mn_I atom in the Mn_1Ga_3 interstitial position slightly improves agreement with the experiment for high-energy part of the spectrum above 1118 eV but still does not reproduce negative major peak at the 1116 eV. It is interesting to note that

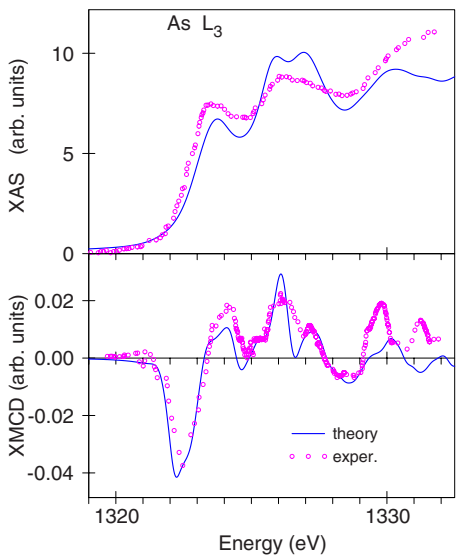

FIG. 6. (Color online) X-ray absorption (top panel) and XMCD (bottom panel) spectra of (Ga,Mn)As at the As L_3 edge calculated in the LSDA approximation (full line) and the experimentally measured (Ref. 57) (circles) from a $x=0.07$ sample.

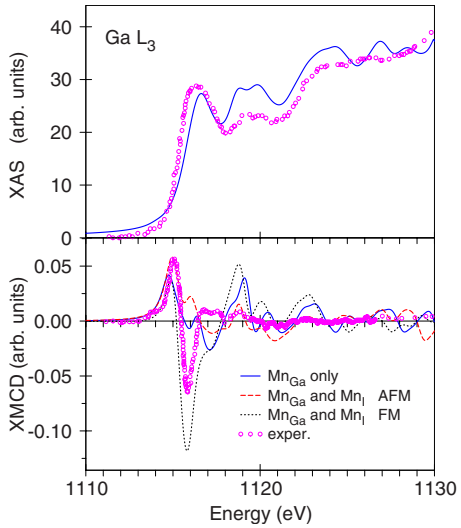

FIG. 7. (Color online) The experimentally measured x-ray absorption (top panel) and XMCD (bottom panel) (Ref. 57) spectra of (Ga,Mn)As at the Ga L_3 edge (circles) and the LSDA calculation with only one Mn_{Ga} substituted atom (full lines) and with an additional Mn_I atom in the Mn_1Ga_3 interstitial position with antiferromagnetic (dashed line) and ferromagnetic (dotted line) ordering to the Mn_{Ga}.

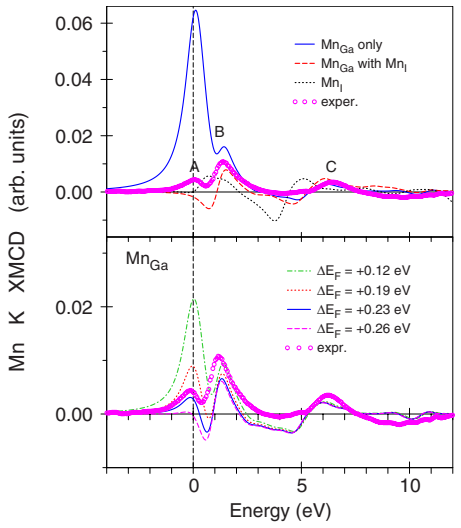

FIG. 8. (Color online) Top panel: Mn K XMCD experimental spectrum (Ref. 66) (circles) and theoretical calculations for a 64-atom GaAs unit cell containing one substituted Mn_{Ga} atom (full line), two atoms in the unit cell (Mn_{Ga} and Mn_I) at the Mn_{Ga} (dashed line), and one interstitial Mn_I site (dotted line). Bottom panel: Mn K XMCD experimental spectrum (Ref. 66) (circles) and theoretical calculations with one substituted Mn_{Ga} atom with artificially shifted Fermi level.

this peak appears under assumption of the ferromagnetic alignment of Mn_{Ga} and Mn_I moments (dotted line). We present in Fig. 7 only the L_3 XAS and XMCD spectra. Similar results were obtained also for the spectra at the Ga L_2 edge, where the sign of the XMCD signal is opposite to the L_3 one.

3. XMCD spectra at the K edges

The XAS and XMCD spectra in metals and alloys at the K edge in which the $1s$ core electrons are excited to p states through the dipolar transition are quite important. They are sensitive to the electronic states at neighboring sites because of the delocalized nature of the p states. It has been documented that sizable XMCD signals can be detected at the K edge of nonmagnetic atoms, such as sulfur, oxygen, and nitrogen in ferromagnetic EuS,[101] EuO,[102] and GdN.[103,104]

The XMCD at the Mn K edge in the (Ga,Mn)As DMS was measured in an external magnetic field of ± 2 T by Freeman *et al.* (Ref. 66). Figure 8 shows the Mn K XMCD spectrum calculated in the LSDA approach together with the experimental data.[66] The prominent part of the Mn XMCD consists of a double-peak structure (A and B) with a splitting of 1.4 eV and smaller positive fine structure (C) at around 6 eV above the Fermi level. As may be seen from the upper panel of Fig. 8 the theory fails to reproduce the experimentally measured spectrum with either a single substitutional Mn_{Ga} in the 64-atom GaAs unit cell or with an additional interstitial Mn_I atom in the Mn_1Ga_3 position. For the single substitutional atom the theory strongly overestimates the intensity of the first low-energy peak A while in the latter case the theory does not produce the peak A at all. However, the third peak C is well reproduced in both these cases.

Freeman *et al.* (Ref. 66) associated the first low-energy peak A with the electric quadrupole $1s \rightarrow 3d$ transitions. We checked this possibility by calculating the electric quadrupole E_2 and magnetic dipole M_1 transitions for the Mn K XAS and XMCD spectra. We found that the M_1 transitions are extremely small in comparison with the E_2 transitions and can be neglected. The E_2 transitions are much weaker than the electric-dipole transitions E_1 and they are almost invisible in the XAS. The intensity of the quadrupole E_2 transitions does not exceed 1% in the whole energy range of the XMCD spectrum. We also investigated the core-hole effect on the final states. When the $1s$ core electron is photoexcited to the unoccupied p states, the charge distribution changes in order to screen the created hole. We found that the final-state interaction has a minor influence on the shape of the Mn K XMCD spectrum. The influence of electronic correlations on the Mn K XMCD spectrum was investigated within the rotationally invariant LSDA+U approach[86] with U applied only to the Mn d states. Its main effect is to increase the splitting between the occupied majority- and unoccupied minority-spin Mn states. This causes some increase in the Mn spin magnetic moment from the LSDA value of $3.751\mu_B$–$4.269\mu_B$. However, the intensity of the A peak changes very little (not shown).

To analyze the situation in more details we present in Fig. 9 the density of Mn p states calculated within the LSDA for the 64-atom GaAs unit cell at the Mn_{Ga} site with only one substituted Mn atom (a) and with an additional Mn interstitial at the Mn_1Ga_3 site for the Mn_{Ga} (b), and Mn_I (c) sites. From the top panel of Fig. 9 we may conclude that the contribution to the prominent peak A comes from the transitions from the $1s$ core level to the $N_p(E)$ peak situated at the Fermi level. The second prominent peak B arises from the transi-

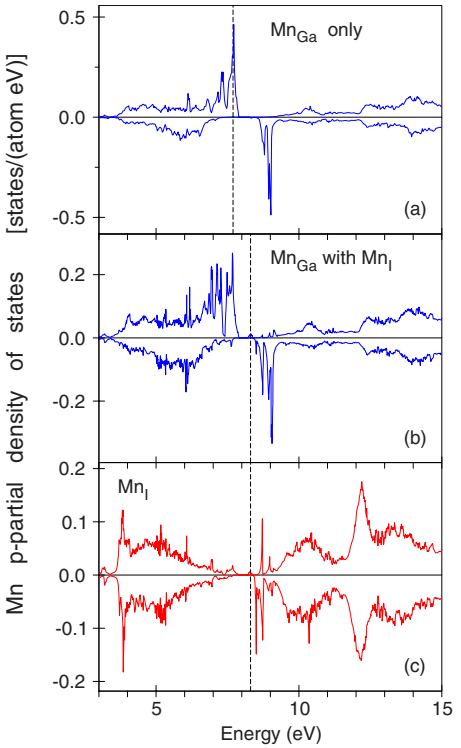

FIG. 9. (Color online) The Mn p partial density of states [in states/(atom eV)] in the LSDA approximation calculated for the 64-atom GaAs unit cell at the: (a) Mn_{Ga} site with only one substitution Mn atom; (b) Mn_{Ga} site with an additional Mn atom in the Mn_1Ga_3 interstitial position; and (c) Mn_I site at the Mn_1Ga_3 position. The Fermi energy is shown by the vertical dashed line.

tions to the minority p DOS at 1.4 eV above the Fermi level. By comparing the top and the middle panels in Fig. 9 we may conclude that the donor Mn_I interstitial atom shifts the Fermi energy upward by approximately 0.6 eV. The prominent peak at the Fermi level become fully occupied and lies far below the Fermi level. As a result, the specific transitions do not take place at small photon energies anymore and the peak structure A disappears from the calculated XMCD spectrum.

As we already discussed above, the calculations with one Mn_I atom in the unit cell correspond to a 50% concentration of the interstitial atoms and greatly overestimate the typical experimental concentrations. One would expect much smaller shift of the Fermi level for realistic concentrations of Mn_I. To calculate the band structure of the (Ga,Mn)As DMS for a realistic concentration of the interstitial atoms (1–5 %) one has to construct an enormously large supercells which exceeds our present ability. Therefore to model small concentration of the interstitial atoms we use the rigid-band approximation by shifting artificially the Fermi level upward. As may be seen from the bottom panel of Fig. 8 the intensity of the prominent peak A rapidly decreases with increasing ε_F and actually disappears for $\Delta\varepsilon_F$=+0.26 eV when all the Mn p states closed to the Fermi level became fully occupied.

It is worthwhile comparing the energy distribution of the Mn $3d$ (Figs. 3 and 4) with the p (Fig. 9) partial DOSs. In the case of a single Mn_{Ga} atom in the unit cell the Mn $3d$ partial DOS has a relatively small peak of the majority spin t_2 states at the Fermi level and two strong minority-spin peaks of e and t_2 symmetry above the Fermi energy. On the other hand, the p DOS in this case has quite a large peak at the Fermi level and only one strong minority unoccupied peak as a result of t_2-p hybridization. The corresponding partial DOSs for the Mn_I atom are also quite different: the Mn $3d$ partial DOS has a strong narrow peak right at the Fermi energy in the spin-up channel but there is no such a peak in the p states. The different energy distributions of the Mn $3d$ and p partial DOSs play essential role in the different shapes of the Mn K and $L_{2,3}$ XMCD spectra. Besides, the K and $L_{2,3}$ XMCD spectra are determined by different interactions. The XMCD spectra at the $L_{2,3}$ edges are mostly determined by the strength of the SO coupling of the initial $2p$ core states and spin polarization of the final empty $3d_{3/2,5/2}$ states while the exchange splitting of the $2p$ core states as well as the SO coupling of the $3d$ valence states are less important.[105] However, the SO coupling and the exchange splitting of the final p states is mostly responsible for the observed dichroism at the Mn, As, and Ga K edges because the exchange splitting of the initial $1s$-core state is extremely small. Actually a XMCD K spectrum reflects the orbital polarization of the p states in differential form $d\langle l_z\rangle/dE$.[106,107] We calculated the site-dependent function $dm_{tl}(E) = \Sigma_{n\mathbf{k}}\langle\Psi_{tl}^{n\mathbf{k}}|\hat{l}_z|\Psi_{tl}^{n\mathbf{k}}\rangle\delta(E-E_{n\mathbf{k}})$,[108] where $\hat{l}_z$ is the z—projection of the angular momentum operator, $E_{n\mathbf{k}}$ and $\Psi_{tl}^{n\mathbf{k}}$ are the energy of the nth band and the part of the corresponding LMTO wave function formed by the states with the angular momentum l inside the atomic sphere centered at the site t, respectively. In analogy with the l-projected density of states, $dm_{tl}(E)$ may be referred to as the site and l projected density of the expectation value of $\hat{l}_z$. This quantity has a purely relativistic origin and when the SO interaction is equal to zero $dm_{tl}(E)\equiv 0$. The orbital moment M_l at the site t is given by $M_{tl}(E)=\int_{E_b}^{E_F} dm_{tl}(E)dE$, where E_b is the bottom of the valence band. As may be seen in the top panel of Fig. 10 the K XMCD spectrum and $dm_{tl}(E)$ function are indeed closely related to one another giving a rather simple and straightforward interpretation of the XMCD spectra at the K edge.

We have studied the influence of the SO coupling and the exchange splitting on the Mn K XMCD spectrum by scaling the corresponding terms in the Hamiltonian artificially with a constant prefactor. This was done in a nonself-consistent way, i.e., after self-consistency had been achieved, only one iteration was performed with the modified Hamiltonian. From the resulting band structure the XMCD spectra were then computed. These modifications can in addition be done atom dependent, i.e., within each atomic sphere so that one can investigate the separate effects of these quantities on Mn, As, and Ga.

The outcomes of these model calculations for the Mn K XMCD spectrum of (Ga,Mn)As are shown in Fig. 10. In the middle panel, the importance of the exchange splitting is illustrated. As expected when the exchange splitting on As or Ga is set to zero, the dichroism changes very little. But when the exchange splitting on Mn is set to zero the XMCD vanishes nearly completely. This implies that the exchange splitting due to Mn is crucial for the sizeable dichroism at the Mn K edge but that of As and Ga is unimportant.

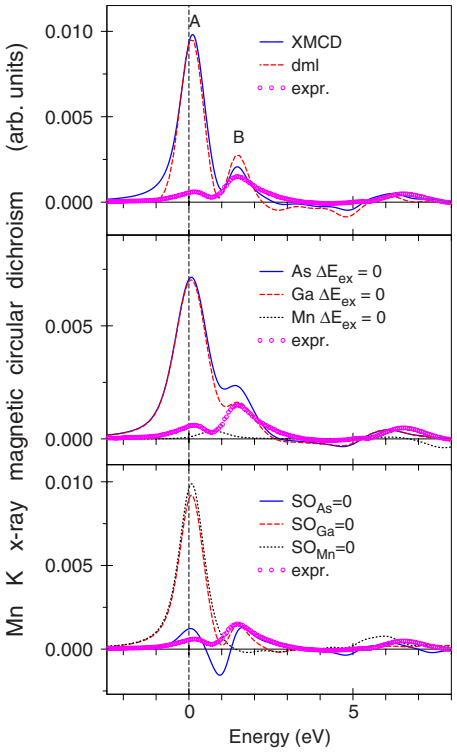

FIG. 10. (Color online) Top panel: Mn *K* XMCD experimental spectrum (Ref. 66) (circles) and the theoretically calculated ones for a 64-atom GaAs unit cell containing one substituted Mn_{Ga} atom (full line); the dashed line presents the $dm_{l=1}(E)$ function (see the explanation in the text). Middle panel: Mn *K* XMCD experimental spectrum (Ref. 66) (circles) and the theoretically calculated ones for the exchange splitting at the As, Ga, and Mn sites set to zero (full, dashed, and dotted lines, respectively). Bottom panel: Mn *K* XMCD experimental spectrum (Ref. 66) (circles) and the theoretically calculated ones with spin-orbit splitting at the As, Ga, and Mn sites set to zero (full, dashed, and dotted lines, respectively).

The bottom panel of Fig. 10 shows the XMCD dependence on the SO coupling. If we set the SO coupling on Ga to zero, the XMCD spectrum does not change (dashed line). When the SO coupling on Mn is zero, the high-energy peak *B* completely disappears (dotted line). On the other hand, if we set the SO coupling on As to zero, the peak *B* does not change, however, the peak *A* is strongly reduced. Thus, the SO coupling of Mn is responsible for the large dichroism in the peak *B* while the SO of As produces the large circular dichroism near the Mn *K* edge (peak *A*). The exchange splitting of Mn is mostly responsible for the dichroism signal in both the peaks.

The XMCD at the Ga and As *K* edges in the (Ga,Mn)As DMS were investigated experimentally by Freeman *et al.* (Ref. 66). A clear dichroism was observed at the onset of the As absorption edge. The dichroism at the Ga *K* edge was found to be much weaker and scarcely visible above the noise level. Figure 11 (top panel) shows the isotropic x-ray absorption spectrum of As at the *K* edge calculated in the LSDA approach together with the experimental data.[66] There is some small disagreement in the relative intensities of the fine structures in the region of the major x-ray absorption.

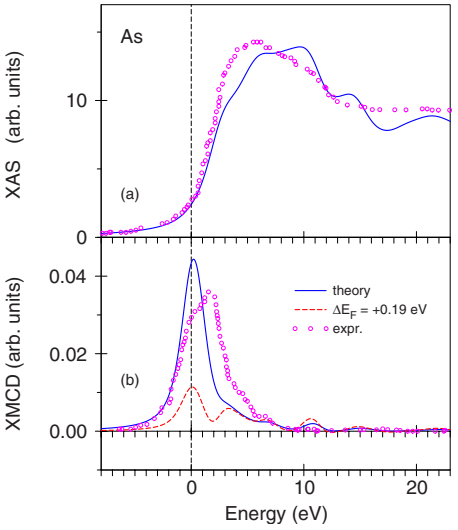

FIG. 11. (Color online) (a) the experimentally measured (Ref. 66) (circles) x-ray absorption spectrum of (Ga,Mn)As at the As *K* edge and the theoretically calculated one for a 64-atom GaAs unit cell containing one substituted Mn_{Ga} atom (full line) and (b) the experimentally measured (Ref. 66) (circles) and the theoretically calculated (full line) XMCD spectra of (Ga,Mn)As at the As *K* edge. Dashed line shows the calculated spectrum with artificially shifted Fermi level.

The theory also shows more pronounced fine structures for As XAS spectrum above 10 eV.

The LSDA calculations describe reasonably well the shape of the As *K* XMCD spectrum (bottom panel of Fig. 11). However, the theory places the major XMCD peak right at the *K* edge. The experimentally measured As *K* spectrum has a shoulder at the edge with the major peak shifted upward by around 1.4 eV. There is also an additional high-energy shoulder at around 5 eV above the edge. The origin of such a disagreement has the same nature as described above in connection with the Mn *K* XMCD spectrum. The existence of additional impurity donor Mn_I atoms shifts the Fermi level upward. Figure 11 presents the As *K* XMCD spectrum with the Fermi energy shifted by 0.19 eV. In the latter case the intensity of the peak at the *K* edge is reduced and the second structure at higher energy appears. The explanation presented here has only qualitative character and for a quantitative examination one should prepare the supercell calculations for a realistic concentration of the Mn_I atoms.

We have also studied the influence of the SO coupling and the exchange splitting on the As *K* XMCD spectrum. The top panel of Fig. 12 illustrates the importance of the exchange splitting. When the exchange splitting on As or Ga is set to zero, the dichroism hardly changes. But when the exchange splitting on Mn is set to zero the XMCD almost vanishes. This implies that the exchange splitting at Mn site is crucial for a sizeable dichroism at the As *K* edge due to the Mn 3*d*-As 4*p* hybridization.

The bottom panel of Fig. 12 shows the dependence of the As *K* XMCD on the SO coupling. If we set the SO coupling on Ga or Mn to zero, the XMCD spectrum hardly changes (dashed and dotted lines, respectively). When the SO cou-

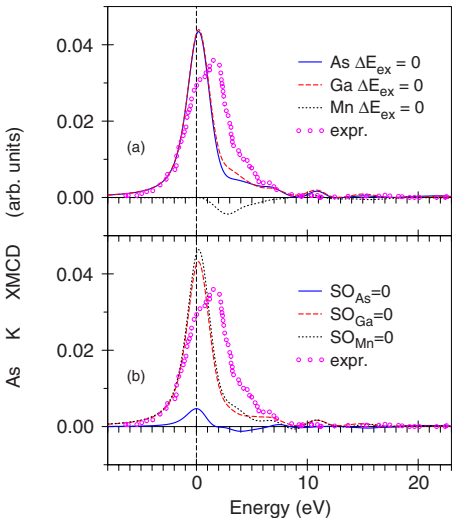

FIG. 12. (Color online) (a) The experimentally measured (Ref. 66) (circles) XMCD spectrum of (Ga,Mn)As at the As K edge and the theoretically calculated ones for exchange splitting at the As, Ga, and Mn sites set to zero (full, dashed, and dotted lines, respectively) and (b) the experimentally measured (Ref. 66) (circles) XMCD spectrum of (Ga,Mn)As at the As K edge and the theoretically calculated ones with spin-orbit splitting at the As, Ga, and Mn sites set to zero (full, dashed, and dotted lines, respectively).

pling on As is zero, the dichroism almost vanishes (full line). This indicates that the SO interaction in the $4p$ states and the exchange splitting at Mn site are responsible for the large dichroism at the As K edge.

B. (GaMn)N DMS

1. Energy band structure

Figure 13 presents total and partial density of states for a 36-atom GaN wurtzite unit cell containing one Mn_{Ga} substitution (x=0.06) in the LSDA. The (Ga,Mn)N DMS has the electronic structure of a half-metal with the energy gap in the minority spin channel. The N s states are located mostly between −16.9 and −13.9 eV below the Fermi level and the s states of the Ga are situated between −8 eV and −6 eV. The p states of Ga and N strongly overlap and occupy the −8.3 to −1.3 eV energy range. The spin splitting of the Ga and N p states is quite small.

The crystal field at the Mn_{Ga} site (C_{3v} point symmetry) causes the splitting of Mn d orbitals into a singlet $a_1(3z^2-1)$ and two doublets e (xy and x^2-y^2) and e_1 (yz and xz). The majority-spin Mn a_1 narrow peak is situated in close vicinity to the Fermi energy (see insert in the bottom panel of Fig. 13), the corresponding minority DOSs are between 2 and 2.2 eV above the Fermi level. The electronic states of e symmetry ranges from −1.45 to −1.0 and 1.15 to 1.45 eV for majority and minority spins, respectively. The hole states just above the Fermi level up to 0.3 eV for spin-up are due to the e states. There is a strong hybridization between Mn $3d$ and N $2p$ states at the top of the valence band.

The magnetic moment in the (Ga,Mn)N unit cell is equal to $4\mu_B$ an integer consistent with the half-metalicity seen in the DOS. Our band-structure calculations produce the spin magnetic moment of $3.466\mu_B$ at the Mn_{Ga} in the $(Ga_{1-x}Mn_x)N$ (x=0.06). The induced magnetic moments at the N first-neighbor sites are parallel to that of the Mn ions (with spin magnetic moments about $0.042\mu_B$ and $0.064\mu_B$ for longer and shorter distant N atoms, respectively). Twelve Ga ions in the second-neighbor shell couple ferromagnetically to the substituted Mn ion with spin magnetic moments from $0.013\mu_B$ to $0.019\mu_B$. The orbital moments at the Ga and N sites are small with the largest one at the N first-neighbor sites ($0.005\mu_B$). The orbital magnetic moment at the Mn_{Ga} site is equal to $-0.040\mu_B$ and antiparallel to the spin moment. This observation is in contrast with (Ga,Mn)As for which a small positive Mn orbital moment was obtained (see).

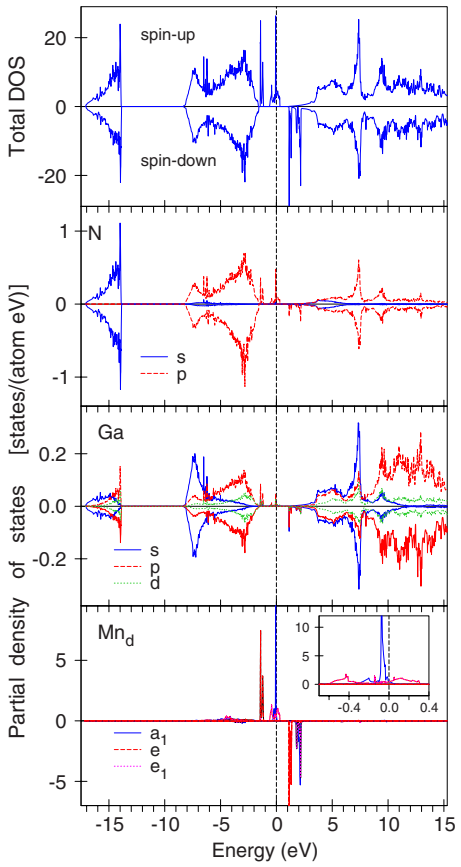

FIG. 13. (Color online) The LSDA total [in states/(cell eV)] and partial [in states/(atom eV)] density of states of the $(Ga_{1-x}Mn_x)N$ (x=0.06) for wurtzite-type crystal structure. The inset is a blowup of the PDOS of Mn close to the Fermi energy. The Fermi energy is at zero.

2. XMCD spectra

The x-ray absorption and x-ray magnetic circular and linear dichroism of the dilute magnetic semiconductor (Ga,Mn)N at the Ga and Mn K edges have been investigated by Sarigiannidou *et al.* (Refs. 15 and 70). Figure 14 shows x-ray absorption spectra recorded for two orthogonal polarizations at the Ga K edge and their difference (XLD), for (Ga,Mn)N with 6.3% Mn in comparison with the theoretical

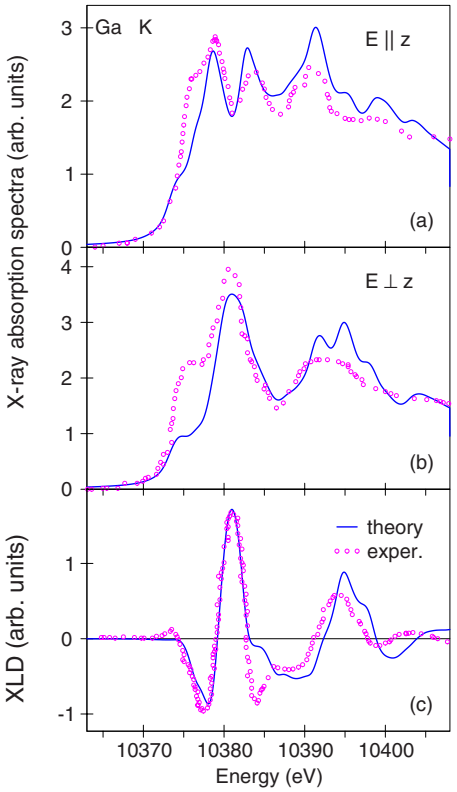

FIG. 14. (Color online) Theoretically calculated (full line) and the experimentally measured (Ref. 15) (circles) XAS of (Ga,Mn)N at the Ga K edge for linearly polarized x-ray light oriented (a) parallel and (b) perpendicular to the c axis; (c) theoretically calculated (full line) and experimental (Ref. 15) (circles) XLD spectra at the Ga K edge.

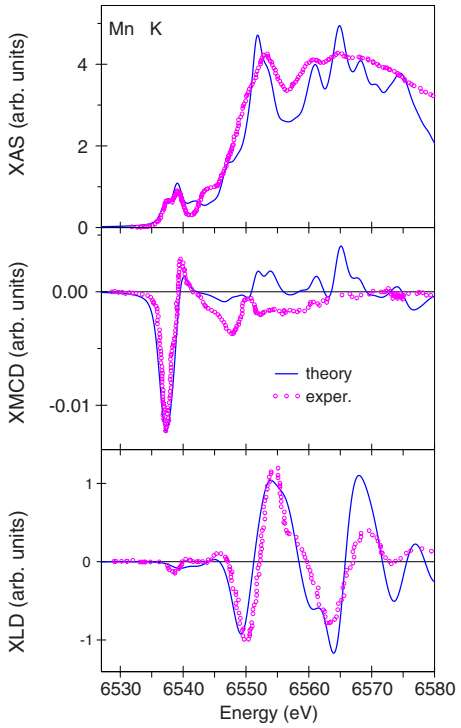

FIG. 15. (Color online) Top panel: theoretically calculated (full line) and the experimentally measured (Ref. 15) (circles) isotropic XAS of (Ga,Mn)N at the Mn K edge. Middle panel: theoretically calculated (full line) and experimental (Ref. 15) (circles) XMCD spectra at the Mn K edge. Bottom panel: theoretically calculated (full line) and experimental (Ref. 15) (circles) XLD spectra at the Mn K edge.

LSDA calculations. The theory reproduces the shape of XAS and XLD spectra very well. There is small disagreement between the theory and the experiment in the relative intensities of the prominent peaks of the x-ray absorption spectra. Also, the theoretically calculated high-energy peak in the XLD spectrum at around 10 395 eV is slightly shifted to higher energies in comparison with the measurement.

Figure 15 presents the theoretically calculated isotropic XAS as well as XMCD spectra of (Ga,Mn)N at the Mn K edge in comparison with the experiment by Sarigiannidou *et al.* (Ref. 15). The theory correctly describes the energy position and relative intensities of all the fine structure in the x-ray emission spectrum including the two low-energy peaks near the edge. The experimentally measured Mn K XMCD spectrum has a very intense signal (1.6% with respect to the step at the edge) in close vicinity to the edge. The theory reproduces the major negative peak near the edge well but slightly underestimates the second positive peak at about 6540 eV. The agreement between the theory and the experiment for the XLD spectrum at the Mn K edge is also quite good (Fig. 15). The oscillatory behavior of the high-energy part of the theoretical XLD and XMCD spectra at the Mn K edge could possibly be damped by quasiparticle lifetime effects, which is not taken into account in our calculations.

The XAS and XMCD spectra of the (Ga,Mn)N DMS at the Mn $L_{2,3}$ edges were measured by Freeman *et al.*[71] and Kevney *et al.* (Ref. 13). Freeman *et al.*[71] measured two wurtzite and two zinc-blende (Ga,Mn)N samples using both fluorescent yield and total electron yield detection modes. It should be noticed that FY gives increased sensitivity to the bulk of the layers (probing depth is $\sim$10–100 nm, compared to $\sim$3 nm for TEY) but is prone to saturation effects due to the comparable mean-free paths of incoming and outgoing photons. This can lead to distortion of the spectra by suppression of the most intense peaks.[71] The Mn flux used during growth by Freeman *et al.*[71] corresponds to a 2–3 % Mn content, which was the same for all samples. However, the Mn incorporation may not be the same for the different host structure types, and the XA spectra for the wurtzite samples give a higher integrated intensity than the zinc-blende samples (up to twice as large), indicating a greater amount of incorporated Mn atoms. For all samples studied, the XMCD L_3 peak is found to be split into two components, the lower energy peak (denoted A) and the higher-energy peak (denoted B), separated by about 0.85 eV. The relative intensities of each peak vary from sample to sample. Zinc-blende samples produce a more pronounce double-peak structure than wurtzite samples.

In Ref. 13, peaks A and B were ascribed to isolated substitutional Mn^{2+} and to Mn^{2+} neighboring an interstitial N ion, respectively. Freeman *et al.*[71] suggest that peak A is associated with bulk Mn^{2+} states (d^5 configuration) and peak B to Mn surface states with the configuration between d^5 and

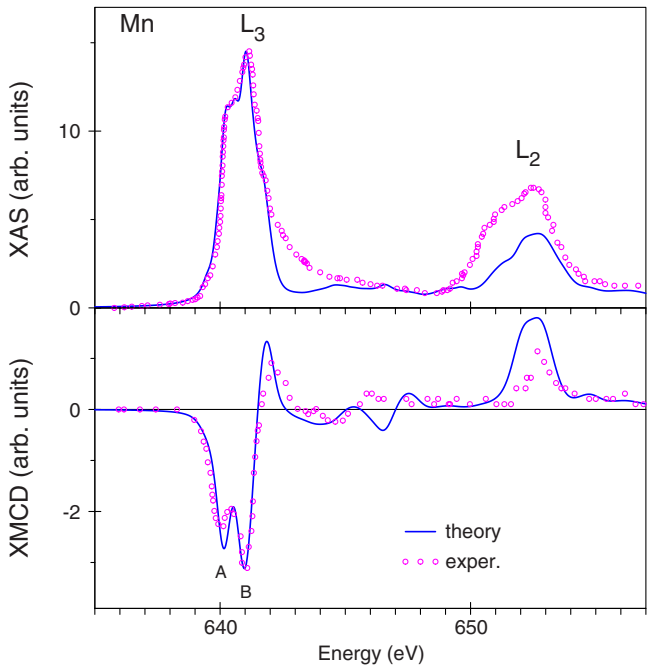

FIG. 16. (Color online) Top panel: theoretically calculated (full line) and experimentally measured (Ref. 71) (circles) x-ray absorption spectra of (Ga,Mn)N at the Mn $L_{2,3}$ edges for the wurtzite structure. The experimental spectra were measured with an external magnetic field of 5 T using the fluorescent yield detection mode at 10 K. Bottom panel: theoretically calculated (full line) and experimental (Ref. 71) (circles) XMCD spectra of (Ga,Mn)N at the Mn $L_{2,3}$ edges.

d^4. Indeed, the comparison of the measured spectra to atomic multiplet calculations[71] reveals that the shift of 0.85 eV between the two peaks corresponds to roughly half that expected between atomic d^4 and d^5 configurations. Moreover, the calculated multiplet structure for d^4 Mn does not fully agree with the experimental spectrum. Therefore they associate peak B to some hybridized d^4-d^5 states.

From the itinerant band-structure picture we may suggest a simpler and more straightforward explanation of the peaks A and B. Figure 16 shows the isotropic x-ray absorption and XMCD spectra of Mn at the $L_{2,3}$ edges calculated in the LSDA approach together with the experimental data for the wurtzite structure. The theory produces a double-peak structure for the Mn $L_{2,3}$ XAS and XMCD spectra both in the wurtzite and zinc-blende (not shown) structures. The peak A arises from $2p \rightarrow e$ transitions in both the structures. The peak B is due to $2p \rightarrow t_2$ and $2p \rightarrow (a_1, e_1)$ transitions for the wurtzite and cubic zinc-blende structures, respectively. In agreement with the experiments,[71] we found a more pronounced double-peak structure in the XAS and XMCD Mn L_3 spectra for the cubic zinc-blende structure (x=0.03) than for the wurtzite structure (x=0.06) due to higher crystal symmetry and lower concentration of Mn_{Ga} atoms in the former case.

C. (Ga,Gd)N DMS

1. Energy band structure

Figure 17 presents partial density of states for a 36-atom GaN wurtzite unit cell containing one Gd_{Ga} substitution (x=0.06) in the LSDA and LSDA+U approximations. The (Ga,Gd)N is a semiconductor with the energy gap of about 1.25 eV. The minority 4f states overlap with the Ga and N p states from 4.4 to 5.3 eV above the Fermi level. In the LSDA+U calculations the Coulomb U_{eff} applied to the 4f states increases the splitting between the occupied majority- and unoccupied minority-spin Gd states. This causes a small increase in the Gd spin magnetic moment from the LSDA value of $6.605\mu_B$–$6.861\mu_B$. The occupied LSDA+U majority Gd 4f states became much broader due to the overlap and hybridization with the Gd 5d states. However, the minority empty 4f states did almost not change only shifted upward by 0.9 eV. We found a quite small Gd 4f-5d hybridization above the Fermi level.

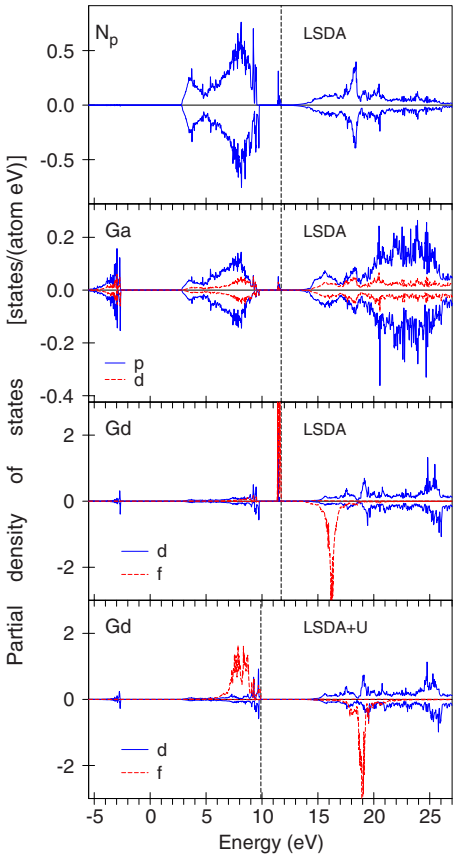

FIG. 17. (Color online) The partial density of states [in states/(atom eV)] of $(Ga_{1-x}Gd_x)N$ (x=0.06) for the wurtzite-type crystal structure in the LSDA and LSDA+U approach.

2. XMCD spectra

The XLD in (Ga,Gd)N DMSs at the Ga K and Gd L_3 edges have been measured by Martinez-Criado *et al.* (Ref. 72) and Ney *et al.* (Ref. 73). The XMCD spectra at the Gd L_3 edge was also detected by Ney *et al.* (Ref. 73).

Figure 18 shows x-ray absorption spectra for two orthogonal polarizations, and their difference (XLD), at the Ga K edge for (Ga,Gd)N DMS in comparison with the theoretical calculations in the LSDA and LSDA+U approximations. The LSDA and LSDA+U Ga K spectra are almost identical due to the small hybridization between empty Gd 4f and 5p

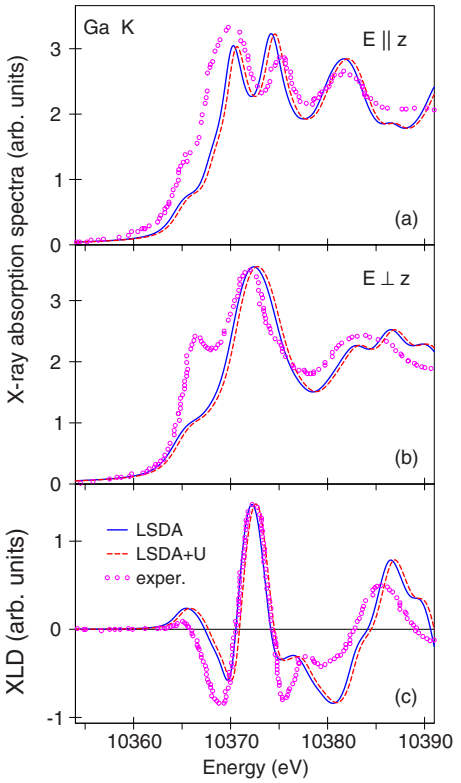

FIG. 18. (Color online) The theoretically calculated in the LSDA (full lines) and LSDA+U (dashed lines) approximations in comparison with the experimentally measured (Ref. 73) (circles) x-ray absorption spectra of (Ga,Gd)N with wurtzite structure at the Ga K edge for linearly polarized x-ray-light-oriented (a) parallel and (b) perpendicular to the c axis; (c) theoretically calculated in the LSDA (full line) and LSDA+U (dashed line) approximations and experimental (Ref. 73) (circles) XLD spectra at the Ga K edge.

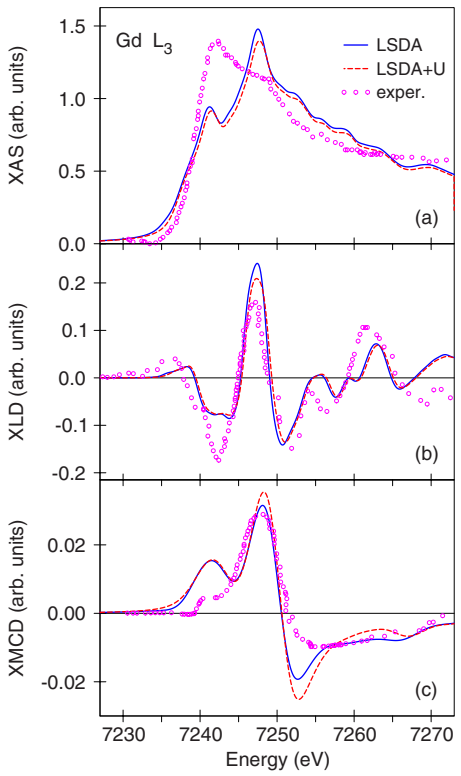

FIG. 19. (Color online) (a) theoretically calculated in the LSDA (full line) and LSDA+U (dashed line) approximations and the experimentally measured (Ref. 73) (circles) isotropic x-ray absorption spectra of (Ga,Gd)N in the wurtzite structure at the Gd L_3 edge; (b) theoretically calculated in the LSDA (full line) and LSDA+U (dashed line) approximations and experimental (Ref. 73) (circles) XLD spectra at the Gd L_3 edge; and (c) theoretically calculated in the LSDA (full line) and LSDA+U (dashed line) approximations and the experimental (Ref. 15) (circles) XMCD spectra at the Gd L_3 edge.

valence states. The spectral shape of the Ga K XAS and XLD spectra is very similar to that observed in the (Ga,Mn)N DMS (compare Figs. 14 and 18). In both cases the theory reproduces the spectra quite well with slightly better agreement with the measured spectra for the (Ga,Mn)N DMS.

Figure 19 shows x-ray absorption spectra as well as XLD and XMCD spectra at the Gd L_3 edge for (Ga,Gd)N in comparison with the theoretical calculations in the LSDA and LSDA+U approximations. The theory reproduces the experimentally measured XLD spectrum at the Gd L_3 edge well. In the case of the XMCD spectrum the theory overestimates the low-energy shoulder near the edge at around 7241 eV. The LSDA and LSDA+U approximations produce similar results indicating that the spectral shape of the XAS and dichroism spectra only depend weakly on the energy position of the Gd $4f$ states due to the small hybridization between empty Gd $4f$ and $5d$ states.

Figure 20 presents theoretically calculated XLD and XMCD spectra at the N K edge for the (Ga,Mn)N and (Ga,Gd)N DMSs. We predict a quite large linear and circular dichroism at the N K edge. The XLD spectra have complicated spectral shape in both the (Ga,Mn)N and (Ga,Gd)N DMSs. The linear dichroism is one order of magnitude larger than the circular one. Circular dichroism was found to be much larger in the Mn-substituted GaN than in the Gd-substituted one. We calculated the K XMCD spectrum at the N site with turned off spin-orbit interaction (SOI) separately on the N $2p$ states and at the Mn site. We found that the K XMCD spectrum is slightly changed when the SOI on the N site is turned off while the spectrum almost disappears (intensity reduced almost 2 order of magnitude) when the SOI on the Mn site is turned off. This indicates that the SOI on the Mn site is influencing the orbital mixture of N $2p$ states through the N $2p$-Mn $3d$ hybridization. A similar situation was found in (Ga,Gd)N where the N $2p$-Gd $4f$ hybridization plays a crucial role for the N K edge XMCD. Both the cases differ from (Ga,Mn)As DMS where the SO interaction in the As $4p$ states together with the exchange splitting at Mn site play a major role for the circular dichroism at the As K edge (see Sec. III). The experimental measurements of the XLD and XMCD spectra in the Mn- and Gd-substituted GaN at the N K edge would be highly desirable.

V. SUMMARY

We have studied the electronic structure and x-ray magnetic circular and linear dichroism of the (Ga,Mn)As-,

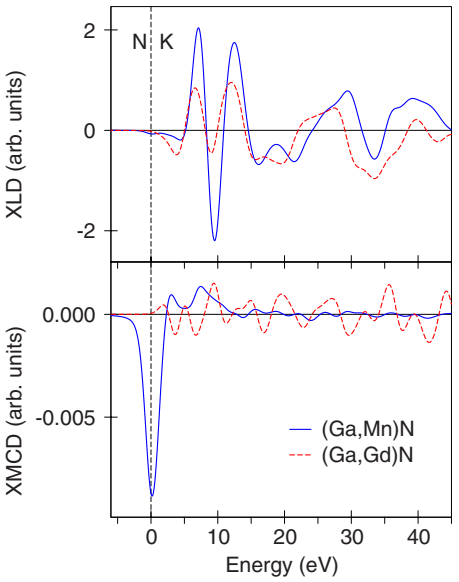

FIG. 20. (Color online) Theoretically calculated XLD (top panel) and XMCD (bottom panel) spectra at N K edge for the (Ga,Mn)N (full lines) and (Ga,Gd)N (dashed lines) DMSs.

(Ga,Mn)N-, and (Ga,Gd)N-diluted magnetic semiconductors by means of *ab initio* fully-relativistic spin-polarized Dirac linear muffin-tin orbital method in the framework of the LSDA and LSDA+U approximations. The absorption and the dichroism spectra at the Mn, As, Ga, and N K and Gd, Mn, As, and Ga $L_{2,3}$ edges were investigated.

At high hole densities, Mn has a tendency to autocompensate by occupying donor interstitial sites. From total energy band-structure calculations we found that the lowest energy has the configuration with Mn_I ions occupying the tetragonal positions surrounded by three Ga and one Mn_{Ga} near neighbor. The Mn_I is antiferromagnetically coupled with the Mn_{Ga} ion.

The theory reproduces the shape and energy positions of major fine structures of the Mn XASs and XMCD spectra at the $L_{2,3}$ edges in (Ga,Mn)As DMS reasonably well. However it does not produce the low-energy positive peak at around 636 eV. This structure was found to be due to interband transitions from the $2p$ core level to the $3d$ majority empty state of t_2 symmetry situated at the Fermi level at the Mn_I site. We found quite small anisotropy for the x-ray magnetic circular dichroism and giant anisotropy for the linear dichroism at the Mn $L_{2,3}$ edges in agreement with the measurements by Edmonds *et al.* (Ref. 62) and Freeman *et al.* (Ref. 63). We show that the exchange splitting of the initial Mn $2p_{1/2,3/2}$ core levels is responsible for the huge XMLD at the Mn $L_{2,3}$ edges and its strong angular dependence.

The prominent part of the Mn K XMCD spectrum in the (Ga,Mn)As DMS consists of a double-peak structure (A and B) with a splitting of 1.4 eV. We found that the SO coupling of Mn is responsible for the large dichroism in peak B and the SO of As produces the large circular dichroism near the Mn K edge (peak A). The exchange splitting of Mn is to the greatest extent responsible for the dichroism signal in both peaks. We found that the core-hole effect in the final states and quadrupole E_2 transitions has a minor influence on the shape of the Mn K XMCD spectrum. The shape of the Mn and As K XMCD spectra might be explain only taking into account the existence of the interstitial Mn_I atoms. The exchange splitting at the Mn site and the SO interaction at the As site responsible for large x-ray circular dichroism at the As K edge.

The LSDA calculations produce a double-peak structure of the Mn $L_{2,3}$ XAS and XMCD spectra of the (Ga,Mn)N DMS both in the wurtzite and zinc-blende-type structures. Peak A arises from $2p \rightarrow e$ transitions in both the structures. Peak B is due to the $2p \rightarrow t_2$ and $2p \rightarrow (a_1, e_1)$ transitions for wurtzite and cubic zinc-blende structures, respectively. We found a small hybridization between empty Gd $4f$ and $5d$ states in the (Ga,Mn)N DMS, for this reason the XAS, XLD, and XMCD spectra at the Gd L_3 edge are very similar in the LSDA and LSDA+U calculations.

The theoretically calculated linear and circular dichroism at the N K edge are significant. The circular dichroism was found to be much larger in the Mn-substituted GaN than in the Gd-substituted one. The N $2p$-Mn $3d$ hybridization in the (Ga,Mn)N and N N $2p$-Gd $4f$ one in the (Ga,Gd)N DMSs play a crucial role for the N K edge XMCD dichroism but minor role of the SO interaction in the N $2p$ states.

ACKNOWLEDGMENTS

The authors are indebted to S. Ostanin from the Max Planck Institute of Microstructure Physics at Halle for providing the optimized crystal structure calculations of the (Ga,Mn)As DMS using VASP-SGGA method and helpful discussions. V.N.A. gratefully acknowledges the hospitality at Max-Planck-Institut für Festkörperforschung in Stuttgart during his stay there. This work was supported by Science and Technology Center in Ukraine (STCU) under Project No. 4930.

[1] J. K. Furdyna, J. Appl. Phys. **64**, R29 (1988).
[2] S. Sanvito, G. Theurich, and N. A. Hill, J. Supercond. **15**, 85 (2002).
[3] T. Jungwirth, J. Sinova, J. Masek, J. Kucera, and A. H. MacDonald, Rev. Mod. Phys. **78**, 809 (2006).
[4] S. J. Potashnik, K. C. Ku, R. Mahendiran, S. H. Chun, R. F. Wang, N. Samarth, and P. Schiffer, Phys. Rev. B **66**, 012408 (2002).
[5] P. M. Krstajic, F. M. Peeters, V. A. Ivanov, V. Fleurov, and K. Kikoin, Phys. Rev. B **70**, 195215 (2004).
[6] T. Dietl, H. Ohno, F. Matsukura, J. Cibert, and D. Ferrand, Science **287**, 1019 (2000).
[7] M. Zajac, J. Gosk, M. Kaminska, A. Twardowski, T. Szyszko, and S. Podsiadlo, Appl. Phys. Lett. **79**, 2432 (2001).

[8] M. Zajac, R. Doradzinski, J. Gosk, J. Szczytko, M. Lefeld-Sosnowska, M. Kaminska, A. Twardowski, M. Palczewska, E. Grzanka, and W. Gebicki, Appl. Phys. Lett. **78**, 1276 (2001).
[9] M. E. Overberg, C. R. Abernathy, S. J. Pearton, N. A. Theodoropoulou, K. T. McCarthy, and A. F. Hebard, Appl. Phys. Lett. **79**, 1312 (2001).
[10] M. L. Reed, N. A. El-Masry, H. H. Stadelmaier, M. K. Ritums, and M. J. Reed, Appl. Phys. Lett. **79**, 3473 (2001).
[11] T. Sasaki, S. Sonoda, Y. Yamamoto, K. I. Suga, S. Shimizu, K. Kindo, and H. Hori, J. Appl. Phys. **91**, 7911 (2002).
[12] S. J. Pearton, C. R. Abernathy, M. E. Overberg, G. T. Thaler, D. P. Norton, N. Theodoropoulou, A. F. Hebard, Y. D. Park, F. Ren, J. Kim, and L. A. Boatner, J. Appl. Phys. **93**, 1 (2003).
[13] D. J. Keavney, S. H. Cheung, S. T. King, M. Weinert, and L. Li, Phys. Rev. Lett. **95**, 257201 (2005).
[14] J. I. Hwang, Y. Ishida, M. Kobayashi, Y. Osafune, T. Mizokawa, A. Fujimori, Y. Takeda, K. Terai, S. I. Fujimori, Y. Saitoh, Y. Muramatsu, A. Tanaka, T. Kondo, H. Munekata, M. Hashimoto, H. Tanaka, S. Hasegawa, and H. Asahi, Phys. Status Solidi B **243**, 1696 (2006).
[15] E. Sarigiannidou, F. Wilhelm, E. Monroy, R. M. Galera, E. Bellet-Amalric, A. Rogalev, J. Goulon, J. Cibert, and H. Mariette, Phys. Rev. B **74**, 041306(R) (2006).
[16] I. T. Yoon, M. H. Ham, and J. M. Myoung, Appl. Surf. Sci. **255**, 4840 (2009).
[17] K. Sato and H. Katayama-Yoshida, Jpn. J. Appl. Phys. **40**, L485 (2001).
[18] M. van Schilfgaarde and O. N. Mryasov, Phys. Rev. B **63**, 233205 (2001).
[19] L. Kronik, M. Jain, and J. R. Chelikowsky, Phys. Rev. B **66**, 041203(R) (2002).
[20] M. Wierzbowska, D. Sanchez-Portal, and S. Sanvito, Phys. Rev. B **70**, 235209 (2004).
[21] A. Filippetti, N. A. Spaldin, and S. Sanvito, Chem. Phys. **309**, 59 (2005).
[22] L. M. Sandratskii, P. Bruno, and J. Kudrnovsky, Phys. Rev. B **69**, 195203 (2004).
[23] P. Mahadevan and A. Zunger, Appl. Phys. Lett. **85**, 2860 (2004).
[24] X. Luo and R. M. Martin, Phys. Rev. B **72**, 035212 (2005).
[25] J. L. Xu, M. van Schilfgaarde, and G. D. Samolyuk, Phys. Rev. Lett. **94**, 097201 (2005).
[26] T. C. Schulthess, W. M. Temmerman, Z. Szotek, W. H. Butler, and G. M. Stocks, Nat. Mater. **4**, 838 (2005).
[27] Y. H. Chang, C. H. Park, K. Sato, and H. Katayama-Yoshida, J. Korean Phys. Soc. **49**, 203 (2006).
[28] Y. H. Chang, C. H. Park, K. Sato, and H. Katayama-Yoshida, Phys. Rev. B **76**, 125211 (2007).
[29] Z. S. Popovic, S. Satpathy, and W. C. Mitchel, Phys. Rev. B **70**, 161308(R) (2004).
[30] B. Sanyal, O. Bengone, and S. Mirbt, Phys. Rev. B **68**, 205210 (2003).
[31] E. Kulatov, H. Nakayama, H. Mariette, H. Ohta, and Y. A. Uspenskii, Phys. Rev. B **66**, 045203 (2002).
[32] A. Titov, X. Biquard, D. Halley, S. Kuroda, E. Bellet-Amalric, H. Mariette, J. Cibert, A. E. Merad, G. Merad, M. B. Kanoun, E. Kulatov, and Yu. A. Uspenskii, Phys. Rev. B **72**, 115209 (2005).
[33] S. Dhar, O. Brandt, A. Trampert, L. Daweritz, K. J. Friedland, K. H. Ploog, J. Keller, B. Beschoten, and G. Gunterodt, Appl. Phys. Lett. **82**, 2077 (2003).
[34] N. Teraguchi, A. Suzuki, Y. Nanishi, Y.-K. Zhou, M. Hashimoto, and H. Asahi, Solid State Commun. **122**, 651 (2002).
[35] S. Dhar, O. Brandt, M. Ramsteiner, V. F. Sapega, and K. H. Ploog, Phys. Rev. Lett. **94**, 037205 (2005).
[36] H. Asahi, Y. K. Zhou, M. Hashimoto, M. S. Kim, X. J. Li, S. Emura, and S. Hasegawa, J. Phys.: Condens. Matter **16**, S5555 (2004).
[37] G. M. Dalpian and S.-H. Wei, Phys. Rev. B **72**, 115201 (2005).
[38] J. Hite, G. T. Thaler, R. Khanna, C. R. Abernathy, S. J. Pearton, J. H. Park, A. J. Steckl, and J. M. Zavada, Appl. Phys. Lett. **89**, 132119 (2006).
[39] K. Kikoin, Low Temp. Phys. **35**, 58 (2009).
[40] A. Ernst, L. M. Sandratskii, M. Bouhassoune, J. Henk, and M. Lüders, Phys. Rev. Lett. **95**, 237207 (2005).
[41] J. H. Park, S. K. Kwon, and B. I. Min, Physica B **281-282**, 703 (2000).
[42] S. C. Erwin and A. G. Petukhov, Phys. Rev. Lett. **89**, 227201 (2002).
[43] F. Maca and J. Masek, Phys. Rev. B **65**, 235209 (2002).
[44] K. Sato, P. H. Dederics, and H. Katayama-Yoshida, Europhys. Lett. **61**, 403 (2003).
[45] G. Bouzerar, J. Kudrnovsky, L. Bergqvist, and P. Bruno, Phys. Rev. B **68**, 081203(R) (2003).
[46] S. C. Erwin and C. S. Hellberg, Phys. Rev. B **68**, 245206 (2003).
[47] J.-S. Filhol, R. Jones, M. J. Shaw, and P. R. Briddon, Appl. Phys. Lett. **84**, 2841 (2004).
[48] J. Kudrnovsky, I. Turek, V. Drchal, F. Maca, P. Weinberger, and P. Bruno, Phys. Rev. B **69**, 115208 (2004).
[49] K. W. Edmonds, P. Boguslawski, K. Y. Wang, R. P. Campion, S. N. Novikov, N. R. S. Farley, B. L. Gallagher, C. T. Foxon, M. Sawicki, T. Dietl, M. Buongiorno Nardelli, and J. Bernholc, Phys. Rev. Lett. **92**, 037201 (2004).
[50] A. B. Shick, J. Kudrnovsky, and V. Drchal, Phys. Rev. B **69**, 125207 (2004).
[51] R. Wu, Phys. Rev. Lett. **94**, 207201 (2005).
[52] J. Kudrnovsky, G. Bouzerar, and I. Turek, Appl. Phys. Lett. **91**, 102509 (2007).
[53] B. Beschoten, P. A. Crowell, I. Malajovich, D. D. Awschalom, F. Matsukura, A. Shen, and H. Ohno, Phys. Rev. Lett. **83**, 3073 (1999).
[54] H. Ohldag, V. Solinus, F. U. Hillebrecht, J. B. Goedkoop, M. Finazzi, F. Matsukura, and H. Ohno, Appl. Phys. Lett. **76**, 2928 (2000).
[55] S. Ueda, S. Imada, T. Muro, Y. Saitoh, S. Suga, F. Matsukura, and H. Ohno, Physica E (Amsterdam) **10**, 210 (2001).
[56] Y. Ishiwata, M. Watanabe, R. Eguchi, T. Takeuchi, Y. Harada, A. Chainani, S. Shin, T. Hayashi, Y. Hashimoto, S. Katsumoto, and Y. Iye, Phys. Rev. B **65**, 233201 (2002).
[57] D. J. Keavney, D. Wu, J. W. Freeland, E. Johnston-Halperin, D. D. Awschalom, and J. Shi, Phys. Rev. Lett. **91**, 187203 (2003).
[58] K. W. Edmonds, N. R. S. Farley, R. P. Campion, C. T. Foxon, and B. L. Gallagher, Appl. Phys. Lett. **84**, 4065 (2004).
[59] K. W. Edmonds, N. R. S. Farley, T. K. Johal, G. van der Laan, R. P. Campion, B. L. Gallagher, and C. T. Foxon, Phys. Rev. B **71**, 064418 (2005).
[60] O. Rader, K. Fauth, C. Gould, C. Ruster, G. Schott, G. Schmidt, K. Brunner, L. Molenkamp, G. Schutz, F. Kronast, H. A. Dürr, W. Eberhardt, and W. Gudat, J. Electron Spectrosc. Relat. Phenom. **144-147**, 789 (2005).

[61] T. Jungwirth, J. Masek, K. Y. Wang, K. W. Edmonds, M. Sawicki, M. Polini, J. Sinova, A. H. MacDonald, R. P. Campion, L. X. Zhao, N. R. S. Farley, T. K. Johal, G. van der Laan, C. T. Foxon, and B. L. Gallagher, Phys. Rev. B **73**, 165205 (2006).
[62] K. W. Edmonds, G. van der Laan, A. Freeman, N. R. S. Farley, T. K. Johal, R. P. Campion, C. T. Foxon, B. L. Gallagher, and E. Arenholz, Phys. Rev. Lett. **96**, 117207 (2006).
[63] A. A. Freeman, K. W. Edmonds, G. van der Laan, N. R. S. Farley, T. K. Johal, E. Arenholz, R. P. Campion, C. T. Foxon, and B. L. Gallagher, Phys. Rev. B **73**, 233303 (2006).
[64] K. W. Edmonds, A. A. Freeman, N. R. S. Farley, K. Y. Wang, R. P. Campion, B. L. Gallagher, C. T. Foxon, G. van der Laan, and E. Arenholz, J. Appl. Phys. **102**, 023902 (2007).
[65] F. Maccherozzi, G. Panaccione, G. Rossi, M. Hochstrasser, M. Sperl, M. Reinwald, G. Woltersdorf, W. Wegscheider, and C. Back, Surf. Sci. **601**, 4283 (2007).
[66] A. A. Freeman, K. W. Edmonds, G. van der Laan, R. P. Campion, A. W. Rushforth, N. R. S. Farley, T. K. Johal, C. T. Foxon, B. L. Gallagher, A. Rogalev, and F. Wilhelm, Phys. Rev. B **77**, 073304 (2008).
[67] K. W. Edmonds, G. van der Laan, N. R. S. Farley, E. Arenholz, R. P. Campion, C. T. Foxon, and B. L. Gallagher, Phys. Rev. B **77**, 113205 (2008).
[68] Y. Takeda, M. Kobayashi, T. Okane, T. Ohkochi, J. Okamoto, Y. Saitoh, K. Kobayashi, H. Yamagami, A. Fujimori, A. Tanaka, J. Okabayashi, M. Oshima, S. Ohya, P. N. Hai, and M. Tanaka, Phys. Rev. Lett. **100**, 247202 (2008).
[69] J. Kunes and P. M. Oppeneer, Phys. Rev. B **67**, 024431 (2003).
[70] E. Sarigiannidou, E. Monroy, E. Bellet-Amalric, H. Mariette, R. Galera, J. Cibert, F. Wilhelm, and A. Rogalev, Superlattices Microstruct. **40**, 239 (2006).
[71] A. A. Freeman, K. W. Edmonds, N. R. S. Farley, S. V. Novikov, R. P. Campion, C. T. Foxon, B. L. Gallagher, E. Sarigiannidou, and G. van der Laan, Phys. Rev. B **76**, 081201(R) (2007).
[72] G. Martinez-Criado, O. Sancho-Juan, N. Garro, J. A. Sans, A. Cantarero, J. Susini, M. Roever, D.-D. Mai, A. Bedoya-Pinto, J. Malindretos, and A. Rizzi, Appl. Phys. Lett. **93**, 021916 (2008).
[73] A. Ney, T. Kammermeier, E. Manuel, V. Ney, S. Dhar, K. H. Ploog, F. Wilhelm, and A. Rogalev, Appl. Phys. Lett. **90**, 252515 (2007).
[74] M. I. Freiser, IEEE Trans. Magn. **4**, 152 (1968).
[75] J. B. Kortright and S.-K. Kim, Phys. Rev. B **62**, 12216 (2000).
[76] G. Y. Guo, H. Ebert, W. M. Temmerman, and P. J. Durham, Phys. Rev. B **50**, 3861 (1994).
[77] V. N. Antonov, A. I. Bagljuk, A. Y. Perlov, V. V. Nemoshkalenko, V. N. Antonov, O. K. Andersen, and O. Jepsen, Low Temp. Phys. **19**, 494 (1993).
[78] O. K. Andersen, Phys. Rev. B **12**, 3060 (1975).
[79] V. V. Nemoshkalenko, A. E. Krasovskii, V. N. Antonov, V. N. Antonov, U. Fleck, H. Wonn, and P. Ziesche, Phys. Status Solidi B **120**, 283 (1983).
[80] A. Stevenson, Acta Crystallogr., Sect. A: Found. Crystallogr. **50**, 621 (1994).
[81] S. Saib and N. Bouarissa, Physica B **387**, 377 (2007).
[82] J. P. Perdew and Y. Wang, Phys. Rev. B **45**, 13244 (1992).
[83] P. E. Blöchl, O. Jepsen, and O. K. Andersen, Phys. Rev. B **49**, 16223 (1994).
[84] J. L. Campbell and T. Parr, At. Data Nucl. Data Tables **77**, 1 (2001).
[85] V. I. Anisimov, J. Zaanen, and O. K. Andersen, Phys. Rev. B **44**, 943 (1991).
[86] A. N. Yaresko, V. N. Antonov, and P. Fulde, Phys. Rev. B **67**, 155103 (2003).
[87] K. M. Yu, W. Walukiewicz, T. Wojtowicz, I. Kuryliszyn, X. Liu, Y. Sasaki, and J. K. Furdyna, Phys. Rev. B **65**, 201303(R) (2002).
[88] D. Kitchen, A. Richardella, J.-M. Tang, M. E. Flatte, and A. Yazdani, Nature (London) **442**, 436 (2006).
[89] A. M. Yakunin, A. Y. Silov, P. M. Koenraad, J. H. Wolter, W. Van Roy, J. De Boeck, J.-M. Tang, and M. E. Flatte, Phys. Rev. Lett. **92**, 216806 (2004).
[90] A. M. Yakunin, A. Y. Silov, P. M. Koenraad, J.-M. Tang, M. E. Flatte, W. Van Roy, J. De Boeck, and J. H. Wolter, Phys. Rev. Lett. **95**, 256402 (2005).
[91] J. K. Garleff, C. Celebi, W. V. Roy, J.-M. Tang, M. E. Flatte, and P. M. Koenraad, Phys. Rev. B **78**, 075313 (2008).
[92] J. Masek and F. Maca, Phys. Rev. B **69**, 165212 (2004).
[93] S.-H. Wei and S. B. Zhang, Phys. Rev. B **62**, 6944 (2000).
[94] G. M. Dalpian and S.-H. Wei, Phys. Rev. Lett. **93**, 216401 (2004).
[95] M. Jain, L. Kronik, J. R. Chelikowsky, and V. V. Godlevsky, Phys. Rev. B **64**, 245205 (2001).
[96] T. C. Schulthess and W. H. Butler, J. Appl. Phys. **89**, 7021 (2001).
[97] Y.-J. Zhao, W. T. Geng, K. T. Park, and A. J. Freeman, Phys. Rev. B **64**, 035207 (2001).
[98] P. E. Blöchl, Phys. Rev. B **50**, 17953 (1994).
[99] J. P. Perdew, K. Burke, and M. Ernzerhof, Phys. Rev. Lett. **78**, 1396 (1997).
[100] G. Kresse and D. Joubert, Phys. Rev. B **59**, 1758 (1999).
[101] A. Rogalev, J. Goulon, and C. Brouder, J. Phys.: Condens. Matter **11**, 1115 (1999).
[102] P. G. Steeneken, Ph.D. thesis, University of Groningen, 2002.
[103] F. Leuenberger, A. Parge, W. Felsch, K. Fauth, and M. Hessler, Phys. Rev. B **72**, 014427 (2005).
[104] V. N. Antonov, B. N. Harmon, A. N. Yaresko, and A. P. Shpak, Phys. Rev. B **75**, 184422 (2007).
[105] V. Antonov, B. Harmon, and A. Yaresko, *Electronic Structure and Magneto-Optical Properties of Solids* (Kluwer, Dordrecht, 2004).
[106] H. J. Gotsis and P. Strange, J. Phys.: Condens. Matter **6**, 1409 (1994).
[107] M. S. S. Brooks and B. Johansson, in *Spin-Orbit Influenced Spectroscopies*, edited by H. Ebert and G. Schütz (Springer, Berlin, 1996), p. 211.
[108] L. Uba, S. Uba, V. N. Antonov, A. N. Yaresko, T. Slezak, and J. Korecki, Phys. Rev. B **62**, 13731 (2000).